

ELEMENTAL ABUNDANCES OF NEARBY GALAXIES THROUGH HIGH SIGNAL-TO-NOISE RATIO *XMM-NEWTON* OBSERVATIONS OF ULTRALUMINOUS X-RAY SOURCES

LISA M. WINTER

Astronomy Department, University of Maryland, College Park, MD; lwinter@astro.umd.edu

RICHARD F. MUSHOTZKY

Goddard Space Flight Center, Greenbelt, MD; richard@milkyway.gsfc.nasa.gov

AND

CHRISTOPHER S. REYNOLDS

Astronomy Department, University of Maryland, College Park, MD; chris@astro.umd.edu

Received 2006 April 12; accepted 2006 October 12

ABSTRACT

In this paper we examined *XMM-Newton* EPIC spectra of 14 ultraluminous X-ray sources (ULXs) in addition to the *XMM-Newton* RGS spectra of two sources (Holmberg II X-1 and Holmberg IX X-1). We determined oxygen and iron abundances of the host galaxy's ISM using K-shell (O) and L-shell (Fe) X-ray photoionization edges toward these ULXs. We found that the oxygen abundances closely matched recent solar abundances for all of our sources, implying that ULXs live in similar local environments despite the wide range of galaxy host properties. Also, we compare the X-ray hydrogen column densities (n_{H}) for eight ULXs with column densities obtained from radio H I observations. The X-ray model n_{H} values are in good agreement with the H I n_{H} values, implying that the hydrogen absorption toward the ULXs is not local to the source (with the exception of the source M81 XMM1). In order to obtain the column density and abundance values, we fitted the X-ray spectra of the ULXs with a combined power law and one of several accretion disk models. We tested the abundances obtained from the XSPEC models `tbody`, `diskbb`, `grad`, and `diskpn` along with a power law, finding that the abundances were independent of the thermal model used. We comment on the physical implications of these different model fits. We also note that very deep observations allow a breaking of the degeneracy noted by Stobbart and coworkers favoring a high-mass solution for the absorbed `grad`+power-law model.

Subject headings: ISM: abundances — ISM: general — X-rays: ISM

1. INTRODUCTION

Long-exposure *XMM-Newton* observations of nearby galaxies offer new opportunities to study various properties of ultraluminous X-ray source (ULX) spectra. ULXs are bright, nonnuclear X-ray sources with X-ray luminosities $>3 \times 10^{39}$ ergs s^{-1} . In a previous paper (Winter et al. 2006, hereafter Paper I) we analyzed ULX spectra from 32 nearby galaxies. Based on spectral form, luminosity, and location within the optical host galaxy, we classified a population of high/soft-state and low/hard-state ULXs. For the ULXs with the greatest number of counts, the high signal-to-noise ratio (S/N) *XMM-Newton* observations can be analyzed with more than the simple schematic models of our first study (an absorbed power-law and blackbody model for the high state and an absorbed power-law model for the low state). Particularly, the spectra can be used to investigate the properties of absorption along the line of sight to ULXs.

Many similar studies have been done within our own Milky Way, where X-ray absorption models have been used to determine column densities and abundances of the interstellar medium (ISM). The procedure involves spectral fits of absorption features in bright, background X-ray sources. Successful determinations have been made using background galaxy clusters (Baumgartner & Mushotzky 2006) and X-ray binaries (Juett et al. 2004). These studies made use of a bright X-ray source as a background through which they can observe the 542 eV absorption edge produced by photoionization of the inner K-shell electrons of oxygen. Analogous studies have been used in the radio (see Dickey & Lockman 1990) to optical regime, using quasars, supernovae, or stars as a background for hydrogen absorption and 21 cm emission, as a means to measure hydrogen column densities and metal abundances.

In this study we extend the X-ray absorption studies to external galaxies using ULXs. Due to their extreme brightness in the X-ray regime and their nonnuclear location in external galaxies, these sources are ideal for probing the ISM of their host galaxies. Typical ULXs, from our Paper I study, have Galactic line-of-sight column densities of a few times 10^{20} cm^{-2} (Dickey & Lockman 1990) and measured X-ray column densities greater than 10^{21} cm^{-2} (Fig. 8 of Paper I) for the combined ULX and host galaxy. Thus, if the local environment of the ULX contributes little absorption, the X-ray column density is dominated by the host galaxy. One goal of this study is to determine whether this absorption is that of the host galaxy or local ULX environment. Therefore, we compare the X-ray-measured hydrogen column density with H I measurements from alternate methods.

In addition to the brightness of ULXs and the relatively small Milky Way contribution to their X-ray hydrogen column densities, their well characterized X-ray spectra make ULXs ideal for measuring absorption features of the ISM. Bright ULXs (e.g., NGC 1313 X-1) typically have spectra that are well fitted by an absorbed multicomponent blackbody and power-law model. However, there is discussion over whether this standard model is the most physical model for the ULXs (see, for example, Stobbart et al. 2006; Goncalves & Soria 2006). Different models applied to the base ULX spectra can affect the absorption measurements, particularly in the softer part of the spectrum. Thus, in this paper we investigate the effect different soft component models have on the X-ray-measured hydrogen column density and elemental abundances (through the oxygen K-shell edge at 542 eV and the iron L-shell edge at 851 eV).

We use high-S/N *XMM-Newton* observations of ULXs to measure hydrogen column densities and elemental abundances

TABLE 1
DETAILS OF THE ULXs ANALYZED

Source	R.A. ^a	Decl. ^a	$n_{\text{HGAL}}^{\text{b}}$ (10^{20} cm^{-2})	ObsID	Exposure Time ^c (s)	Count Rate ^c (counts s ⁻¹)
NGC 247 XMM1	00 47 03.8	-20 47 46.2	1.54	0110990301	3458, 1389, 1379	0.20, 0.06, 0.06
NGC 253 XMM2	00 47 22.4	-25 20 55.2	1.40	0152020101	..., 10347, 10304	..., 0.08, 0.09
NGC 300 XMM1	00 55 09.9	-37 42 13.9	3.11	0112800101	6778, 2248, 2453	0.19, 0.05, 0.05
M33 X-8	01 33 50.9	+30 39 36.1	5.58	0102640101	11919, 12147, 12142	0.06, 0.02, 0.02
NGC 1313 XMM3	03 18 22.5	-66 36 06.2	4.0	0106860101	6960, 2179, 1793	0.233, 0.08, 0.07
Holm II XMM1	08 19 28.8	+70 42 20.3	3.42	0112520701	31052, 1257, 10807	2.72, 0.76, 0.73
	0200470101	56987,65758, 65766	3.29, 0.95, 0.94
	0200470101	41816, 41802 (RGS)	0.09, 0.11 (RGS)
M81 XMM1	09 55 32.9	+69 00 34.8	4.12	0111800101	50788, ..., 18988	0.51, ..., 0.22
	0200980101	..., 111910, 111930	..., 0.111, 0.104
Hol IX XMM1	09 57 53.3	+69 03 48.7	4.0	0112521001	14976, 6546, 6586	2.07, 0.64, 0.65
	0200980101	104010, 111760, 111830	1.69, 0.51, 0.51
	0200980101	103840, 103830 (RGS)	0.03, 0.04 (RGS)
NGC 4559 X-7	12 35 51.8	+27 56 04	1.51	0152170501	34517, ..., ...	0.318, ..., ...
NGC 4559 X-10	12 35 58.6	+27 57 40.8	1.51	0152170501	34509, ..., ...	0.238, ..., ...
NGC 4631 XMM1	12 41 55.8	+32 32 14	1.28	0110900201	5093, 1969, 1762	0.13, 0.04, 0.04
NGC 5204 XMM1	13 29 38.5	+58 25 03.6	1.42	0142770101	9981, 3352, 3384	0.628, 0.177, 0.179
	0142770301	9231, 2284, 2349	0.855, 0.247, 0.258
M83 XMM1	13 37 19.8	-29 53 49.8	3.94	0110910201	3074, 927, 987	0.12, 0.033, 0.025
NGC 5408 XMM1 ^d	14 03 19.8	-41 22 59.3	5.73	0112290601	5932, 2036, 2077	0.128, 0.032, 0.033

NOTE.—Units of right ascension are hours, minutes, and seconds, and units of declination are degrees, arcminutes, and arcseconds.

^a Right ascension and declination values quoted are the source positions from the EPIC pn images.

^b Milky Way hydrogen column density along the line of sight from Dickey & Lockman (1990).

^c Exposure times and count rates are listed for the EPIC pn, MOS1, MOS2, and RGS (1 and 2), where available. Note that for sources with multiple observations, details for the additional observations are listed below the first observation. Details of the specific RGS (RGS1 and RGS2) observations are indicated with “(RGS)”.

^d A second observation of NGC 5408 XMM1 is referred to in § 4.2. This observation (0302900101) with an exposure time of 130,335 s is proprietary, and an analysis will appear in T. Strohmayer et al. (2007, in preparation).

of oxygen and iron. Located in external galaxies, the X-ray spectral resolution of available ULX spectra is not as good as those of Galactic X-ray binaries, which often have grating spectra available (e.g., Juett et al. 2004). Therefore, in order to be able to distinguish the oxygen K-shell edge as well as the iron L-shell edge located at 851 eV, we needed observations with a large number of counts (≈ 5000 counts). The X-ray observatory *XMM-Newton*, having a larger collecting area than *Chandra*, provides the counts necessary in order to conduct this study. Further, with recent 100 ks *XMM-Newton* observations available for the host galaxies of two well-studied ULXs (Holmberg II and Holmberg IX), these observations allow for the added analysis of Reflection Grating Spectrometer (RGS) spectra in addition to spectra from the European Photon Imaging Cameras (EPIC). The spectral resolution of the EPIC and RGS allows us to test different soft component models for the ULXs, to determine the effect of the model on absorption and abundance measurements.

2. SOURCE SELECTION AND DATA REDUCTION

In Paper I we conducted an archival *XMM-Newton* study of ULXs in 32 nearby (< 8 Mpc) galaxies. As described in that paper, we extracted spectra for the brightest sources in the observations, corresponding to > 400 counts. In this study we chose to further analyze the spectra of the objects with the highest number of counts (> 5000 counts¹). In addition to the 11 sources from Paper I, we include an analysis of three additional sources: the two ULXs in the spiral galaxy NGC 4559 (observation 0152170501)

¹ In Appendices A and B we show results of simulations to determine the number of counts necessary to detect the oxygen and iron absorption edges. We found that $> 40,000$ counts are needed to constrain iron without having large errors in the measurement. For oxygen, > 5000 counts are needed to constrain oxygen without large errors. See Appendices A and B for further details.

and the bright source in M33 (observation 0102640101). A full list of the 14 ULXs, with details of the observations (including exposure times and count rates), is found in Table 1.

The two ULXs in NGC 4559 were originally studied by Vogler et al. (1997) using *Röntgensatellit* (*ROSAT*) and Cropper et al. (2004) with *XMM-Newton*. We follow the naming convention established in these papers. Both of these sources (X-7 and X-10) were not included in Paper I because the host galaxy’s distance is greater than the 8 Mpc limit we initially required. However, we include these sources now due to the high number of counts (> 5000 counts) in their spectra. Initially we did not include M33 X-8 in our ULX survey due to its location in the center of its host galaxy. This source, however, shows no evidence of being a low-luminosity active galactic nucleus and is more likely a black hole X-ray binary (Takano et al. 1994).

Since the initial study of Paper I, longer exposure time *XMM-Newton* observations have become available for three of our sources from the original study. With the permission of Tod Strohmayer, we include data from the 100 ks *XMM-Newton* observation (0200980101) of Holmberg IX. These data include pn and MOS spectra of Holmberg IX XMM1 and MOS spectra of M81 XMM1. We also include a 100 ks *XMM-Newton* observation (0200470101) of Holmberg II XMM1 that became public after the Paper I study. The EPIC and RGS spectra from this observation of Holmberg II XMM1 were first analyzed by Goad et al. (2006). For Holmberg IX XMM1 and Holmberg II XMM1, the 100 ks exposures provided us with the opportunity to extract and analyze, in addition to the EPIC spectra, spectra from the RGS detectors. Thus, we include an analysis of RGS spectra for both Holmberg II XMM1 and Holmberg IX XMM1.

For the EPIC spectra we added to our original sample, we followed the same reduction method as in Paper I. For observations that were processed with an earlier version of the *XMM-Newton*

Science Analysis System (SAS) (we used SAS ver. 6.0²), the observation data files (ODFs) were used to produce calibrated photon event files for the EPIC-MOS and pn cameras using the commands `emchain` and `epchain`. The events tables were filtered using the standard criteria outlined in the *XMM-Newton* ABC Guide. For the MOS data (both MOS1 and MOS2 cameras), good events constitute those with a pulse height in the range of 0.2–12 keV and event patterns that are characterized as 0–12 (single, double, triple, and quadruple pixel events). For the pn camera, only patterns of 0–4 (single and double pixel events) are kept, with the energy range for the pulse height set between 0.2 and 15 keV. The selection expression “FLAG == 0” was used to exclude bad pixels and events too close to the edges of the CCD chips. Time filtering was applied as needed by editing the light curve produced in `xmmselect`. For the EPIC observations, time periods in the observation with high count rates (flares) in the MOS and pn were cut using the command `tabgtigen` with the “RATE<” command set to 5 counts s⁻¹ for MOS detectors and 20 counts s⁻¹ for the pn detector.

We extracted source and background spectra along with response and ancillary response matrices using the SAS task `especget`. The source spectra were extracted from circular regions, typically with radii of 20". This region was adjusted depending on the size of the source and the proximity of the source to either another source or the edge of a CCD chip. We extracted background spectra from annular regions, except when the source was near another source or near the edge of a chip. In this case, in order to avoid source confusion, we extracted background spectra from a circular region located near the source and on the same CCD chip (as for Holmberg IX XMM1 and M81 XMM1).

For the RGS spectra we extracted first- and second-order spectra for the sources Holmberg IX XMM1 (0200980101) and Holmberg II XMM1 (0200470101) using the `rgsproc` command. The right ascension and declination values used to extract the RGS spectra were obtained from the EPIC pn data and are the values quoted in Paper I. Time filtering was applied as for the EPIC data with `tabgtigen`, where the “RATE<” command was set to 0.5 counts s⁻¹ for Holmberg IX and 0.1 counts s⁻¹ for Holmberg II. Once the spectra were obtained, for the RGS as well as EPIC data, they were rebinned to require at least 20 counts bin⁻¹, using the command `grppha` in LHEASOFT.

3. SPECTRAL FITTING

Spectral fitting proceeded using XSPEC version 11.3.1. For the RGS spectra, we simultaneously fitted the first-order spectra from both RGS1 and RGS2 in the RGS band (0.33–2.5 keV). For the EPIC spectra, we fitted the pn and MOS spectra simultaneously in the 0.3–10 keV energy range. We allowed a free normalization constant to account for the differences in flux calibration between the three EPIC cameras. Both the RGS and EPIC spectra were fitted separately.

In the Paper I study we had fitted all of the sources with three standard models: an absorbed power law, an absorbed bremsstrahlung model, and an absorbed combined blackbody and power-law model. We used the XSPEC model `wabs` to account for absorption from the Milky Way and the host galaxy/ULX contribu-

tion. This model is a photoelectric absorption model using the cross sections of Morrison & McCammon (1983) and the solar abundances of Anders & Ebihara (1982). We found that the spectra of the brightest ULXs were typically best fitted by an absorbed combined blackbody and power-law model [fitted in XSPEC as `wabs* wabs* (bbody+pow)` where the first `wabs` model was fitted to the Dickey & Lockman (1990) Milky Way value and the second `wabs` model was fitted to the remaining host galaxy/ULX contribution]. Likewise, we began our study by fitting the additional sources (M33 X-8, NGC 4559 X-7, and NGC 4559 X-10) with the same three models noted above. We found that these sources were well fitted by the absorbed blackbody and power-law model with $\chi^2/\text{dof} \approx 1.0$.

For M33 X-8, the source was well fitted with an absorbed blackbody and power law with best-fit parameters: $n_{\text{H}} = 1.67^{+0.09}_{-0.08} \times 10^{21} \text{ cm}^{-2}$, $kT = 0.74^{+0.02}_{-0.02} \text{ keV}$, $\Gamma = 2.46^{+0.06}_{-0.05}$, and $\chi^2 = 1579.8/1533 \text{ dof}$, where n_{H} represents the host galaxy/ULX hydrogen column (the Milky Way contribution was fixed to the Dickey & Lockman [1990] value listed in Table 1). In Paper I we noted that ULXs well fitted with the combined blackbody and power-law model with a higher disk temperature ($\approx 1 \text{ keV}$) and a lower flux were often well fitted by an absorbed Comptonization model (XSPEC model `compst`). We note that for M33 X-8 the inverse Compton scattering model also fits the data well (`wabs* compst`) but with a $\chi^2 = 1614.9/1536 \text{ dof}$. Despite the larger χ^2 value, the `compst` model better fits the residuals from the spectra's sloping high-energy tail. The best-fit absorbed blackbody and power-law parameters for NGC 4559 X-7 (12^h35^m51.8^s, 27°56'4") were $n_{\text{H}} = 1.51^{+0.04}_{-0.01} \times 10^{21} \text{ cm}^{-2}$, $kT = 0.13^{+0.01}_{-0.02} \text{ keV}$, $\Gamma = 2.16^{+0.10}_{-0.04}$, and $\chi^2 = 410.3/369 \text{ dof}$. For NGC 4559 X-10 (12^h35^m58.6^s, 27°57'40.8") we found $n_{\text{H}} = 1.14^{+0.02}_{-0.01} \times 10^{21} \text{ cm}^{-2}$, $kT = 0.96^{+0.26}_{-0.20} \text{ keV}$, $\Gamma = 2.13^{+0.06}_{-0.05}$, and $\chi^2 = 292.3/330 \text{ dof}$. X-10, as noted in Cropper et al. (2004), is also well fitted by a Comptonization model.

For the sources M33 X-8 and NGC 4559 X-10, we noted that their spectra were well fitted by either an absorbed blackbody and power law or an absorbed Comptonization model. This brings up one issue surrounding ULX spectra, namely, ambiguity over their spectral form. In this paper we assume that there is an analogy between ULXs and Galactic black hole binaries. Thus, we assume that the accurate ULX spectrum for these bright sources is a hard component (well modeled by a power law) and a soft component (which we assume as a thermal contribution from an accretion disk). The form of the soft component, in particular, will affect the measured absorption and abundance values. Thus, an investigation of this component and its effect on the absorption model is important.

The soft component of ULXs is most often modeled as a thermal component originating from an accretion disk surrounding a central black hole. There are numerous disk models applied to model this possibly thermal component. In Paper I we modeled this component as a simple blackbody (in XSPEC `bbody`). While an accretion disk is expected to have a range of temperatures, empirically a single blackbody is a good fit to low-S/N spectra. A simple absorbed blackbody and power-law model was used for Galactic black hole X-ray binaries in the 1980s when the quality of data for these sources was analogous to that for ULXs today. As the next step in accretion disk models, the soft component of ULX spectra is often modeled as an optically thick, geometrically thin, multicomponent blackbody disk (a multicomponent disk or MCD model, `diskbb` in XSPEC; Mitsuda et al. 1984).

Two disk models that are used to fit the soft component of ULX spectra with more physical accuracy are the XSPEC models `diskpn` and `grad`. The `diskpn` model is an extension of the MCD

² Since the original processing of the data in this study, a new version of SAS (6.5) had become available. This version includes updates to the low-energy response files. In Appendices A and B we show results of fitting the pn observations processed with SAS 6.5 (for pn counts >5000). We found that the model parameters are not significantly different between the SAS 6.0 EPIC spectra and SAS 6.5 pn spectra.

TABLE 2
SPECTRAL FITS FOR EPIC SPECTRA WITH THE `tbabs*tbvarabs*edge*(grad+pow)` MODEL

Source	n_{H}^{a} (10^{22} cm^{-2})	O Abundance ^b	Fe Abundance ^b	Mass (M_{\odot})	$\dot{M}/\dot{M}_{\text{Edd}}^{\text{c}}$	Γ	χ^2/dof	Counts ^d
Holm II XMM1	$0.12^{+0.01}_{-0.01}$	$0.90^{+0.11}_{-0.11}$	$0.0^{+0.15}_{-0.0}$	141^{+21}_{-32}	$0.15^{+0.02}_{-0.09}$	$2.36^{+0.05}_{-0.05}$	1.11	342874
	$0.17^{+0.02}_{-0.04}$	$1.27^{+0.23}_{-0.42}$	$3.15^{+1.29}_{-1.74}$	791^{+209}_{-363}	$0.07^{+0.03}_{-0.03}$	$2.29^{+0.07}_{-0.10}$	0.98	43116
Holm IX XMM1	$0.19^{+0.02}_{-0.02}$	$1.34^{+0.12}_{-0.13}$	$2.07^{+0.12}_{-0.13}$	382^{+93}_{-76}	$0.09^{+0.02}_{-0.02}$	$1.38^{+0.25}_{-0.25}$	1.05	148061
	$0.33^{+0.08}_{-0.09}$	$1.38^{+0.29}_{-0.40}$	$3.91^{+1.09}_{-1.86}$	1181^{+1516}_{-719}	$0.11^{+0.20}_{-0.07}$	$1.73^{+0.09}_{-0.09}$	0.64	28108
M33 X-8	$0.20^{+0.04}_{-0.04}$	$1.04^{+0.13}_{-0.18}$	$1.74^{+0.62}_{-0.74}$	$5.24^{+0.38}_{-0.35}$	$1.02^{+0.09}_{-0.08}$	$2.83^{+0.34}_{-0.31}$	0.97	123903
M81 XMM1	$0.66^{+0.11}_{-0.13}$	$1.20^{+0.08}_{-0.10}$	$2.04^{+0.44}_{-0.57}$	$8.61^{+33.58}_{-5.03}$	$2.32^{+44.8}_{-1.31}$	$4.84^{+5.88}_{-0.66}$	1.02	69776
	$0.27^{+0.21}_{-0.09}$	$1.42^{+0.58}_{-0.50}$	$1.67^{+1.61}_{-1.67}$	$4.2^{+7.4}_{-1.8}$	$8.31^{+4.36}_{-5.98}$	$2.08^{+1.58}_{-0.75}$	0.91	31731
NGC 253 XMM2	$0.53^{+0.07}_{-0.12}$	$1.55^{+0.20}_{-0.29}$	$2.73^{+1.17}_{-1.46}$	4140^{+860}_{-2213}	$0.05^{+0.03}_{-0.03}$	$2.32^{+0.10}_{-0.12}$	0.96	20651
NGC 5204 XMM1	$0.10^{+0.04}_{-0.03}$	$1.42^{+0.25}_{-0.75}$	$0.0^{+1.84}_{-0.0}$	464^{+366}_{-219}	$0.04^{+0.08}_{-0.02}$	$1.92^{+0.08}_{-0.08}$	0.96	16717
	$0.13^{+0.05}_{-0.03}$	$0.77^{+0.60}_{-0.77}$	$0.0^{+1.70}_{-0.0}$	445^{+490}_{-217}	$0.06^{+0.12}_{-0.03}$	$2.02^{+0.13}_{-0.14}$	0.93	13864
NGC 1313 XMM3	$0.67^{+0.02}_{-0.04}$	$1.37^{+0.13}_{-0.14}$	$0.0^{+0.34}_{-0.0}$	$5000^{+0.03}_{-1160}$	$0.08^{+0.09}_{-0.02}$	$2.66^{+0.08}_{-0.09}$	1.02	10932
NGC 300 XMM1	$0.15^{+0.05}_{-0.04}$	$2.46^{+0.45}_{-0.43}$	$0.0^{+1.77}_{-0.0}$	417^{+312}_{-175}	$0.02^{+0.03}_{-0.01}$	$2.46^{+0.10}_{-0.11}$	1.01	11479
N4559 X-7	$0.16^{+0.05}_{-0.03}$	$0.46^{+0.53}_{-0.46}$	$0.0^{+1.00}_{-0.0}$	755^{+901}_{-443}	$0.06^{+0.12}_{-0.02}$	$2.10^{+0.10}_{-0.10}$	0.83	12506
NGC 4631 XMM1	$0.28^{+0.06}_{-0.06}$	$0.62^{+0.43}_{-0.58}$	$0.11^{+1.86}_{-0.11}$	$5.2^{+11.4}_{-18.6}$	$0.84^{+0.88}_{-0.42}$	$5.71^{+2.03}_{-0.31}$	1.06	8824
	$0.09^{+0.03}_{-0.03}$	$1.99^{+0.26}_{-0.52}$	$5.0^{+0.0}_{-1.68}$	1477^{+342}_{-477}	$0.10^{+0.15}_{-0.09}$	$2.53^{+0.20}_{-0.16}$	0.96	10045
NGC 4559 X-10	$0.12^{+0.05}_{-0.04}$	$1.28^{+0.61}_{-0.81}$	$0.0^{+2.30}_{-0.0}$	$5.34^{+7.88}_{-2.75}$	$2.74^{+2.52}_{-1.86}$	$2.09^{+0.52}_{-0.28}$	0.77	8837
NGC 247 XMM1	$0.44^{+0.18}_{-0.12}$	$1.09^{+0.35}_{-0.28}$	$0.0^{+1.45}_{-0.0}$	1717^{+3205}_{-929}	$0.05^{+0.02}_{-0.03}$	$3.60^{+6.40}_{-6.60}$	0.60	6226
	$0.13^{+0.09}_{-0.10}$	$1.70^{+1.12}_{-1.65}$	$0.0^{+3.92}_{-0.0}$	$6.34^{+13.4}_{-4.3}$	$0.92^{+0.70}_{-0.70}$	$2.64^{+0.88}_{-0.64}$	0.83	4988

^a Hydrogen column density determined from `tbvarabs`. The Galactic value of n_{H} was fixed to the Dickey & Lockman (1990) value with the `tbabs` model.

^b Element abundance relative to the Wilms solar abundance from the `tbvarabs` model.

^c Ratio of mass accretion rate from the `grad` model to Eddington accretion rate (see § 4).

^d Total number of photon counts from pn and MOS detectors.

(`diskbb`) model, which uses a pseudo-Newtonian potential. The `grad` model (Hanawa 1989; Ebisawa et al. 1991) is a multi-component disk model that, unlike the `diskbb` or `diskpn` model, incorporates the effects of general relativity. One of the advantages of the `grad` model is that it fits the spectra for mass (M_{grad}) and mass accretion rates (\dot{M}) given a few initial assumptions (distance to the source, disk inclination angle, and the ratio of the color temperature to the effective temperature).

In addition to thermal models, other models have been suggested to explain the soft component. Two of these models are ionized reflection and the warm absorber model. Both of these models have been applied to low-redshift PG quasars, sources with blackbody temperatures of 150 eV. This is relevant to ULXs since many spectral fits of ULXs require cool accretion disk temperatures of approximately 100 eV (Kaaret et al. 2003; Miller et al. 2003, 2004; Roberts et al. 2005; Paper I). The reflection model suggests that the soft component results from X-ray-ionized reflection. In this model, backscattering and fluorescence of X-rays in the disk, as well as radiative recombination, cause elements with smaller ionization potentials (e.g., C, O, N) to become highly ionized. Ross & Fabian (2005) note that a relativistically blurred X-ray ionization model folded through an *XMM-Newton* pn response matrix is well fitted by a blackbody with a temperature of 150 eV, the same value that is seen in PG quasars and many ULXs. In the warm absorber model, absorption edges and lines from an absorbing material close to the X-ray source appear as a thermal component in poorer quality spectra. With increased spectral resolution, the numerous absorption edges and lines are distinguishable. The warm absorber may be the result of a strong, mildly relativistic wind from the disk as suggested by Gierliński & Done (2004). Indeed, the presence of a warm absorber is well known and studied in many Seyfert galaxies (e.g., NGC 3783 and MCG -6-30-15).

As noted above, for subsequent spectral fits we assume a thermal model for the soft component of the ULX spectra. In the following section (§ 4) we discuss the effect different thermal models

have on the measured absorption values. In order to measure the hydrogen column density, we fit the spectra of sources listed in Table 1 with the more sophisticated Tuebingen-Boulder ISM absorption model of Wilms et al. (2000) (`tbabs`, `tbvarabs` in XSPEC). This model accounts for X-ray absorption resulting from contributions from X-ray absorption from the gas phase of the ISM, grains, and molecules. The model uses updated solar abundances and photoionization cross sections. For both the EPIC and RGS spectra, we accounted for Galactic hydrogen absorption by setting the column density of the `tbabs` model equal to the Milky Way hydrogen column density along the line of sight to the host galaxy. These column densities are quoted in Table 1 and are all less than $6 \times 10^{20} \text{ cm}^{-2}$.

Since the measured X-ray column densities for ULXs are typically an order of magnitude higher than the Dickey & Lockman (1990) Milky Way values (Fig. 8 of Paper I), we are confident that the additional absorption measured is not from the Milky Way. To determine the host galaxy's hydrogen column density and the abundances of elements along the line of sight (oxygen and iron), we used the `tbvarabs` model. The `tbvarabs` model accounts for X-ray absorption due to photoionization. It includes the effects due to the H_2 molecule and depletion of metals in grains. The model allows for individual fits to abundant elements (He through Ni), H_2 , and depletion of elements in grains. We initially allowed the hydrogen column density to vary, fixing all other `tbvarabs` parameters to their defaults. The Galactic column density remained fixed (using the `tbabs` model), while the other parameters (power-law and blackbody components) were allowed to vary. This was modeled as `tbabs*tbvarabs*(bbody+pow)` in XSPEC, where `tbabs` was fixed to the Milky Way value and `tbvarabs` was used to fit the absorption from the ULX/host galaxy contribution. With the best-fit hydrogen column density (from `tbvarabs`), we allowed the oxygen abundance and then the iron abundance to vary from the solar abundances. Allowing these parameters to float provides measurements of the depth of the oxygen K-shell edge at 542 eV and the iron L-shell edge at 851 eV.

TABLE 3
SPECTRAL FITS FOR RGS SPECTRA WITH THE `tbabs*tbvarabs*edge*(grad+pow)` MODEL

Source	n_{H}^{a} (10^{22} cm^{-2})	O Abundance ^b	Fe Abundance ^b	Mass (M_{\odot})	$\dot{M}/\dot{M}_{\text{Edd}}^{\text{c}}$	Γ	χ^2/dof	Counts ^d
Holm II XMM1	$0.08^{+0.05}_{-0.02}$	$0.65^{+0.61}_{-0.64}$	$0.0^{+1.51}$	147^{+88}_{-83}	$0.24^{+0.11}_{-0.12}$	$1.58^{+6.75}_{-4.58}$	444.4/442	9521
Holm IX XMM1	$0.29^{+0.12}_{-0.08}$	$0.68^{+0.30}_{-0.34}$	$0.36^{+1.36}_{-0.36}$	774^{+4226}_{-570}	$0.09^{+0.16}_{-0.03}$	$1.43^{+0.45}_{-0.98}$	290.4/339	10807

^a Hydrogen column density determined from `tbvarabs`. The Galactic value of n_{H} was fixed to the Dickey & Lockman (1990) value with the `tbabs` model.

^b Element abundance relative to the Wilms solar abundance.

^c Ratio of mass accretion rate from the `grad` model to Eddington accretion rate (see § 4).

^d Total number of photon counts from RGS1 and RGS2 detectors.

As in Baumgartner & Mushotzky (2006), we found that for our 14 sources, the oxygen absorption values from the `tbvarabs` model yielded different values for the EPIC pn and MOS spectra. Thus, we follow the procedure of Baumgartner & Mushotzky (2006) in adding an `edge` model to account for the differences. We add an extra `edge` component to the MOS1 and MOS2 detectors at an energy of 0.53 keV with optical depths of 0.22 and 0.20, respectively [modeled as `tbabs*tbvarabs*edge*(bbody+pow)`].³ This is the template model used for all spectral fits mentioned throughout the rest of the paper, where other thermal models are used in place of the simple blackbody (`bbody`) model as indicated.

An additional problem we note involves the hydrogen column densities along the line of sight. Baumgartner & Mushotzky (2006) note that a column density (n_{H}) greater than $0.5 \times 10^{21} \text{ cm}^{-2}$ is necessary to allow for good oxygen abundance measurements. We also note that at very high n_{H} values the oxygen edge is undetectable, where high absorption values cause the S/N to be too low to detect the edge.

4. NATURE OF THE SOFT COMPONENT

In the previous section we outlined three possible origins for the soft component in ULXs (X-ray reflection, thermal emission from an accretion disk, and a warm absorber model). For our purposes, we assume a thermal component origin. We chose the thermal model since, as described in Paper I, the spectra of ULXs are well described with models used to fit Galactic black hole X-ray binaries. To gauge the effect different disk models (i.e., `bbody`, `diskbb`, `diskpn`, `grad`) may have on the measured abundances, we discuss different disk models in § 4.1. In § 4.3 we assess the usefulness of the model (absorbed disk and power law) for measuring the galactic/ULX hydrogen column density and the oxygen and iron abundances by discussing the physical plausibility of this model.

For sources with at least 5000 counts, the 14 sources listed in Table 1, we fitted the `grad` model for the soft component of the spectra [XSPEC model `tbabs*tbvarabs*edge*(grad+pow)`]. We assumed a disk inclination angle of 60° and a ratio $T_{\text{color}}/T_{\text{eff}} = 1.7$ (the default value, typical of stellar mass BH sources). In Table 2 we list the best-fit parameters for EPIC spectra using this model. Rows with no source name indicated represent an additional observation of the previous ULX (as indicated in Table 1). Table 3 provides the best-fit parameters for the RGS spectra. The important measurements to note are the host galaxy/ULX contribution to the hydrogen column density, oxygen abundance, and iron abundance from the `tbvarabs` model. All errors quoted in this paper are for the 90% confidence level for 1 degree of freedom

³ The edge parameters used by Baumgartner & Mushotzky (2006) were calculated for differences in calibration using SAS ver. 5.4. In Appendices A and B we show that the pn values using SAS 6.5 are consistent with SAS 6.0 pn+MOS derived values. Thus, the correction quoted is valid for our purposes with SAS ver. 6.0.

($\Delta\chi^2 = 2.76$). We provide a representative spectral fit in Figure 1 for the long observation of Holmberg IX XMM1.

4.1. Comparison of Thermal Disk Models

We chose the general relativistic disk model, `grad`, because it is the most physically accurate of the various simple accretion disk models. Also, the `grad` model requires few initial parameters while making a direct calculation of the mass and mass accretion rate of the black hole. In order to compare the `grad` results with an alternate model, we fit the highest S/N observation of Holmberg IX XMM1 with the `diskpn` model (with the inner radius of the disk set to the radius of marginal stability or 6 times the Schwarzschild radius) in place of the `grad` model. We found that the values obtained agreed with those of the `grad` model. The mass from the `diskpn` model was slightly lower at $358 M_{\odot}$ (corresponding to $kT = 0.23 \text{ keV}$), and the iron abundance was slightly higher at 2.33 compared to the `grad` model. Since the `diskpn` and

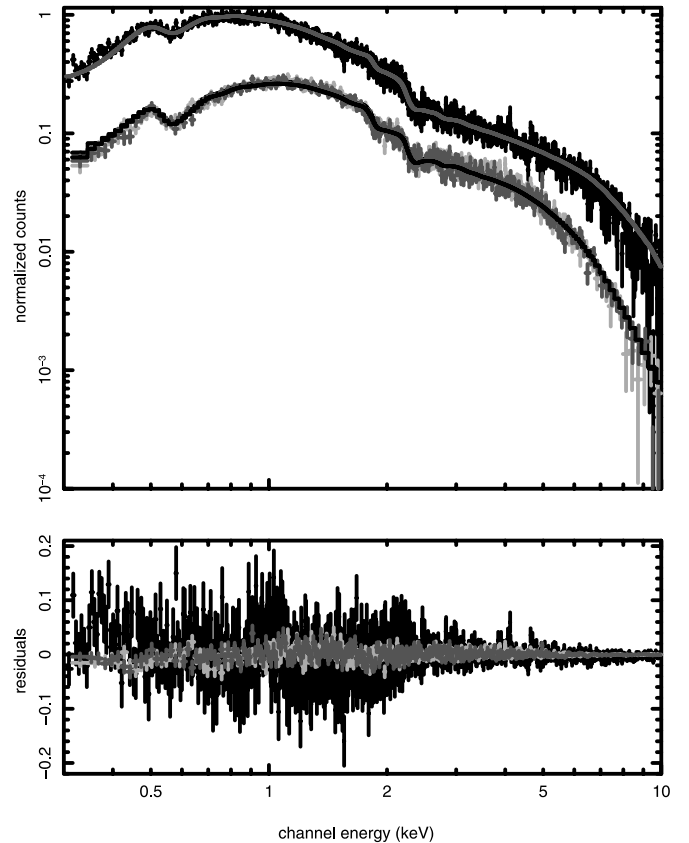


FIG. 1.—EPIC spectrum of observation 0200980101 of Holmberg IX XMM1. This plot shows the spectrum fit with the `tbvarabs*tbabs*edge*(grad+pow)` model and the residuals from this fit. The best-fit parameters are listed in Table 2.

TABLE 4
ALTERNATE THERMAL MODEL SPECTRAL FITS TO ULXs WITH >20,000 COUNTS

Source	n_{H}^{a} (10^{22} cm^{-2})	Oxygen Abundance ^b	Iron Abundance ^b	kT	Γ	χ^2/dof	Counts ^c
tbabs*tbvarabs*edge*(bbody+pow)							
Holm II XMM1	$0.12^{+0.01}_{-0.01}$	$0.97^{+0.11}_{-0.12}$	$0.0^{+0.32}$	$0.24^{+0.01}_{-0.01}$	$2.41^{+0.03}_{-0.03}$	2216.5/2018	342874
	$0.14^{+0.03}_{-0.02}$	$1.37^{+0.38}_{-0.39}$	$4.38^{+0.62}_{-1.8}$	$0.16^{+0.01}_{-0.01}$	$2.31^{+0.08}_{-0.04}$	952.7/973	43116
Holm IX XMM1.....	$0.14^{+0.02}_{-0.01}$	$1.51^{+0.19}_{-0.15}$	$3.37^{+0.99}_{-0.80}$	$0.19^{+0.01}_{-0.01}$	$1.40^{+0.02}_{-0.01}$	2856.7/2752	148061
	$0.23^{+0.10}_{-0.04}$	$1.37^{+0.43}_{-0.44}$	$4.75^{+0.25}_{-1.94}$	$0.17^{+0.02}_{-0.03}$	$1.71^{+0.14}_{-0.06}$	559.5/880	28108
M33 X-8	$0.22^{+0.01}_{-0.14}$	$1.24^{+0.10}_{-0.10}$	$2.38^{+0.31}_{-0.60}$	$0.76^{+0.02}_{-0.02}$	$2.51^{+0.07}_{-0.06}$	1528.8/1533	123903
M81 XMM1.....	$0.39^{+0.03}_{-0.02}$	$1.13^{+0.17}_{-0.07}$	$1.78^{+0.65}_{-0.40}$	$0.90^{+0.03}_{-0.02}$	$2.70^{+0.05}_{-0.05}$	1240.2/1241	69776
	$0.26^{+0.09}_{-0.04}$	$1.46^{+0.26}_{-0.49}$	$1.61^{+2.02}_{-1.61}$	$0.99^{+0.38}_{-0.28}$	$1.76^{+0.13}_{-0.09}$	627.4/668	31731
NGC 253 XMM2	$0.22^{+0.05}_{-0.05}$	$1.21^{+0.40}_{-0.37}$	$1.53^{+1.67}_{-1.53}$	$0.73^{+0.14}_{-0.11}$	$2.16^{+0.08}_{-0.23}$	460.8/496	20651
tbabs*tbvarabs*edge*(diskbb+pow)							
Holm II XMM1	$0.11^{+0.001}_{-0.01}$	$0.65^{+0.09}_{-0.05}$	$0.0^{+0.06}$	$0.34^{+0.02}_{-0.02}$	$2.38^{+0.05}_{-0.04}$	2241.8/2018	342874
	$0.15^{+0.03}_{-0.02}$	$1.05^{+0.34}_{-0.38}$	$2.67^{+1.65}_{-1.71}$	$0.21^{+0.04}_{-0.01}$	$2.27^{+0.06}_{-0.07}$	954.2/973	43116
Holm IX XMM1.....	$0.19^{+0.02}_{-0.02}$	$1.38^{+0.11}_{-0.16}$	$2.39^{+0.58}_{-0.84}$	$0.24^{+0.02}_{-0.01}$	$1.39^{+0.02}_{-0.03}$	2878.9/2752	148061
	$0.30^{+0.11}_{-0.07}$	$1.36^{+0.32}_{-0.38}$	$4.03^{+0.97}_{-1.65}$	$0.20^{+0.04}_{-0.03}$	$1.72^{+0.10}_{-0.07}$	559.8/880	28108
M33 X-8	$0.19^{+0.04}_{-0.03}$	$1.04^{+0.15}_{-0.16}$	$1.75^{+0.68}_{-0.71}$	$1.17^{+0.05}_{-0.05}$	$2.47^{+0.21}_{-0.15}$	1530.4/1533	123903
M81 XMM1.....	$0.63^{+0.08}_{-0.15}$	$1.19^{+0.09}_{-0.15}$	$2.07^{+0.40}_{-0.69}$	$1.38^{+0.03}_{-0.08}$	$4.08^{+0.75}_{-0.59}$	1247.7/1241	69776
	$0.27^{+0.18}_{-0.08}$	$1.42^{+0.57}_{-0.49}$	$1.63^{+1.69}_{-1.63}$	$2.06^{+0.55}_{-0.97}$	$1.98^{+1.40}_{-0.58}$	626.9/668	31731
NGC 253 XMM2	$0.21^{+0.10}_{-0.07}$	$1.16^{+0.53}_{-0.37}$	$1.64^{+1.64}_{-1.64}$	$1.27^{+0.22}_{-0.27}$	$2.27^{+0.83}_{-0.62}$	461.3/496	20651

^a Hydrogen column density determined from tbvarabs. The Galactic value of n_{H} was fixed to the Dickey & Lockman (1990) value with the tbabs model.

^b Element abundance relative to the Wilms solar abundance from the tbvarabs model.

^c Total number of photon counts from pn and MOS detectors.

grad models yield similar values, either of these disk models would be sufficient for determining the hydrogen column density and oxygen and iron abundances.

In order to test the effect the thermal model has on the tbvarabs measured parameters (i.e., n_{H} and abundances), we wanted to compare the results from the more physical disk model (grad) with less physical models (bbody and diskbb). In order to compare the results from these three models, we chose to examine the best-fit parameters for spectra with the highest S/N (using sources with at least 20,000 counts). Thus, in Table 4 we list the best-fit parameters obtained using an absorbed blackbody and power-law [tbabs*tbvarabs*edge*(bbody+pow)] and an absorbed diskbb and power-law model [tbabs*tbvarabs*edge*(diskbb+pow)] for sources with at least 20,000 counts. Subsequently in this paper, when we refer to the bbody, diskbb, or grad models, we are referring to the model fits used in Tables 2–4.

The curvature, or shape of the spectra at low energies, for the bbody, diskbb, and grad models is different, presumably affecting the column density and absorption values. From a comparison of these models, comparing the mean values from all of the observations with >20,000 counts listed in Tables 2 and 4, we find that the column densities obtained with the diskbb model are nearly identical to those with the grad model (the exception is the source NGC 253 XMM2). The MCD (diskbb) model hydrogen column densities are approximately 6% higher than those of the blackbody model (excluding the first M81 XMM1 observation). The average power-law indices for the three models agree within a factor of 5%, with the bbody model having the lowest and the grad having the highest average power-law index (excluding the first M81 XMM1 observation). Thus, the difference in both power-law index and hydrogen column density is negligible on average, with the exceptions of NGC 253 XMM2 and M81 XMM1.

For a comparison of the derived abundances, the oxygen abundance is roughly the same between the grad and bbody model.

These values are approximately 10% higher than those derived from the MCD (diskbb) model. The iron abundances, however, vary more from model to model. The blackbody model average iron abundance is $\approx 13\%$ higher than that of the grad model and $\approx 18\%$ higher than that of the diskbb model. Thus, there are no significant changes to the model parameters in changing the base accretion disk model. These results are verified by simulations described in Appendices A and B.

4.2. Degenerate Model

In modeling our sources with the tbvarabs*tbabs*edge*(grad+pow) model, we found that some of the ULXs were well fitted by a model where the power-law component dominates the low-energy spectrum, also seen in Stobbart et al. (2006). This type of spectral fit typically yields a steeper power-law index ($\Gamma > 3.0$) and a low mass ($M < 10 M_{\odot}$). For two sources, M33 X-8 and M81 XMM1, this model fit was a much better fit than a higher mass model with $\Delta\chi^2$ of 476 and 190, respectively. However, for some sources, there was a degeneracy between the two models (high mass and low mass/steep power law). We illustrate this degeneracy with observation 0112290601 of the source NGC 5408 XMM1, showing the high-mass model and spectral fit in Figure 2 and the low-mass model and spectral fit in Figure 3. For spectra exhibiting this degenerate solution, we include the low-mass/steep power-law fits in Table 5. These fits all exhibit, in addition to low masses, solutions with $\dot{M} \gg \dot{M}_{\text{Edd}}$.

In Stobbart et al. (2006) the authors discussed the same issues in fitting the XMM-Newton spectra of 13 ULXs. They found that two sources, M33 X-8 and NGC 2403 X-1, were best fitted by the model with a power-law fit to the low-energy portion and the thermal model at higher energy. They also indicated six sources where an ambiguity existed between the two models. To understand the spectra of the sources where both models provided good fits to the data, we further investigated the spectra of sources with multiple observations.

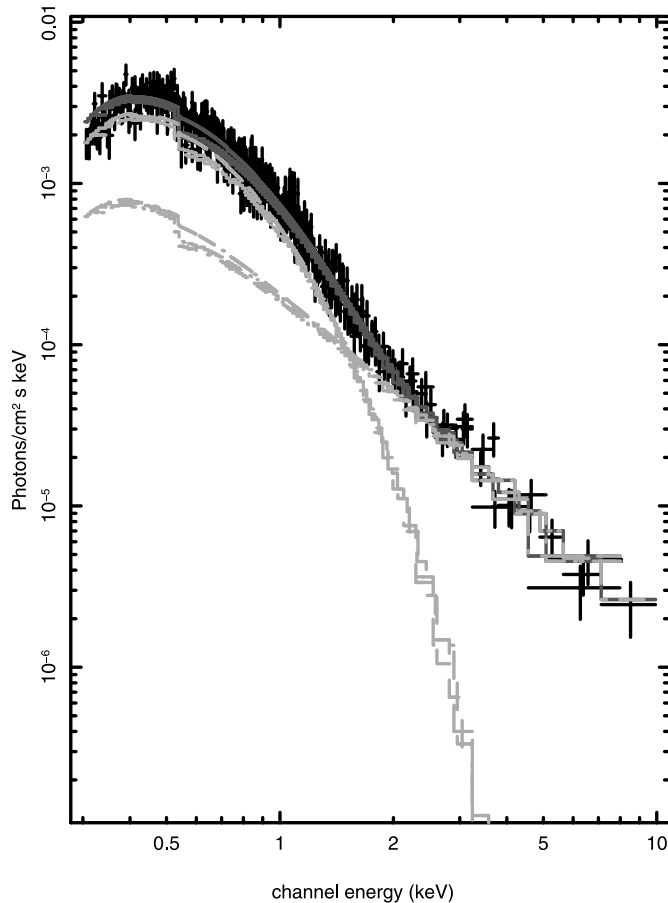


FIG. 2.—Plot of the EPIC unfolded spectrum for the NGC 5408 XMM1 ULX with the high-mass solution (see Table 2). With the spectrum, the absorbed grad and absorbed power-law model components are plotted with light gray lines, while the combined model is plotted in dark gray. The thermal component clearly dominates the low-energy spectrum with this model.

For Holmberg II X-1 and Holmberg IX X-1 our spectral fits include multiple observations (a shorter and a 100 ks observation). For each of these sources, we found that the shorter observation could be fitted with either a high-mass or low-mass solution. When we fitted the 100 ks observation, however, the high-mass model was a much better fit. The $\Delta\chi^2$ values between the high-mass and low-mass solutions for the kilosecond observations were 135 and 88, respectively. To test this further, we also fitted a 100 ks observation of NGC 5408 XMM1 with both of these models. This observation (0302900101) is a proprietary observation whose spectral and temporal analysis will appear in T. Strohmayer et al. (2007, in preparation). We processed the pn data with SAS 6.5, following the same procedure as noted in § 2. Fitting the spectrum with both models (high-mass and low-mass solution), we found a $\Delta\chi^2$ value of 170, favoring the high-mass model.

Thus, we find that for sources that are well fitted by either model (showing a degenerate solution of either high mass or low mass/steep power law) the high-mass solution is the best fit when a higher count spectrum is obtained (as for Holmberg IX XMM1, Holmberg II XMM1, and NGC 5408 X-1). Although we list the alternate model column density and absorption values in Table 5, we use the parameters listed in Table 2 throughout the paper (the high-mass solutions).

As noted, M33 X-8 and M81 XMM1, sources with very high numbers of counts, were not well fitted with a standard disk at low energy, power law at high energy model. They were best fitted with the steep low-energy power-law and hot disk model

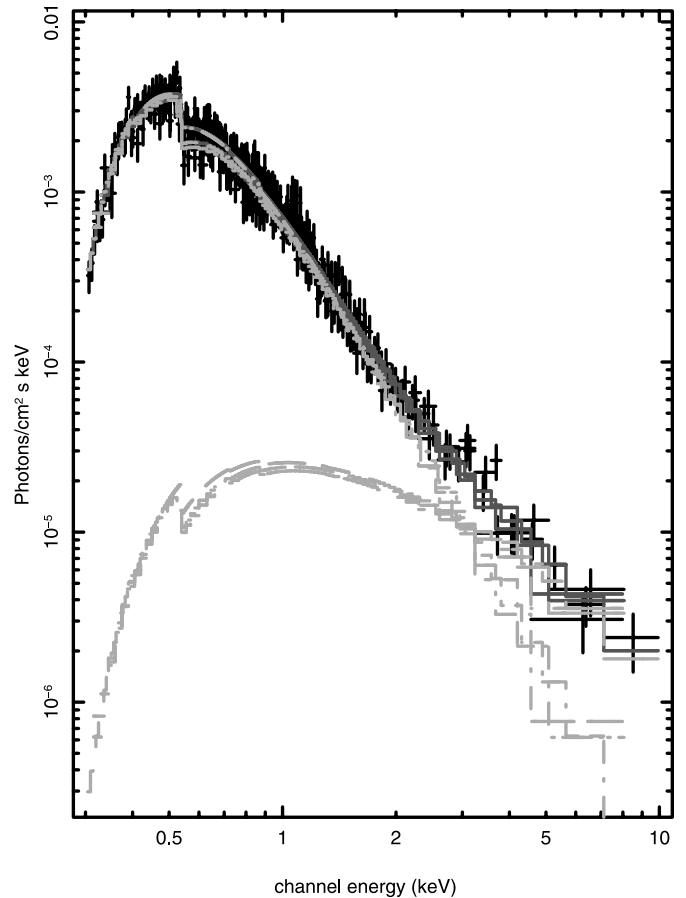


FIG. 3.—Plot of the EPIC unfolded spectrum for the NGC 5408 XMM1 ULX with the low-mass solution (see Table 5). With the spectrum, the absorbed grad and absorbed power-law model components are plotted with light gray lines, while the combined model is plotted in dark gray. Notice that the low-energy spectrum is dominated by the power-law component with a weak contribution from the disk model (grad).

shown in Figure 3. Along with these sources, NGC 4559 X-10 and M83 XMM1 were also well fitted by this model. We further discuss these sources in the following subsection.

4.3. Physical Plausibility of the Accretion Disk Models

In Paper I we had found that ULX spectra are consistent with the high/soft and low/hard states of Galactic black holes. We had classified the sources in this study as consistent with the high/soft state. The high/soft state, as stated earlier, is characterized by emission from an accretion disk and a Comptonized power-law tail. In order to investigate whether the mass and accretion rate results from the grad model make physical sense in terms of the X-ray binary model, we present a comparison of the derived accretion rate in Eddington accretion rate versus the mass in Figure 4. The parameter \dot{M}_{Edd} was computed as $\dot{M}_{\text{Edd}} = (1.3 \times 10^{38} M) / \eta c^2$, where η , the efficiency factor, was set to 0.06 and M is the value M_{grad} . We find that for the sources with $M_{\text{grad}} > 100 M_{\odot}$, the accretion rate is computed to be below 40% of the Eddington rate. This is assuming, as the grad model assumes, a Schwarzschild black hole. Noting that M/\dot{M}_{Edd} is equivalent to L/L_{Edd} for most disk solutions, the L/L_{Edd} values for the sources with $M_{\text{grad}} > 100 M_{\odot}$ are consistent with those of Galactic black hole X-ray binaries in the high state ($L/L_{\text{Edd}} \approx 0.05-1.0$; McClintock et al. 2004). Thus, the sources with $M_{\text{grad}} > 100 M_{\odot}$ do have accretion rates that are predicted from scaling up (in mass) observed high-state Galactic black holes. In addition, the spectral fit parameters

TABLE 5
SPECTRAL FITS FOR EPIC SPECTRA WITH THE `tbabs*tbvarabs*edge*(grad+pow)` MODEL
FOR SOURCES WITH DEGENERATE SOLUTION (LOW MASS/STEEP POWER LAW)

Source	n_{H}^{a} (10^{22} cm^{-2})	O Abundance ^b	Fe Abundance ^b	Mass (M_{\odot})	$\dot{M}/\dot{M}_{\text{Edd}}^{\text{c}}$	Γ	χ^2/dof	Counts ^d
Holm II XMM1	$0.20^{+0.04}_{-0.04}$	$0.83^{+0.17}_{-0.27}$	$1.11^{+0.83}_{-1.11}$	$2.24^{+1.52}_{-1.24}$	$7.79^{+1.52}_{-1.95}$	$3.10^{+0.31}_{-0.30}$	0.99	43116
Holm IX XMM1	$0.39^{+0.13}_{-0.12}$	$1.05^{+0.21}_{-0.33}$	$2.08^{+0.95}_{-1.45}$	$3.91^{+1.47}_{-1.59}$	$22.0^{+1.79}_{-2.86}$	$3.51^{+0.79}_{-0.87}$	0.64	28108
NGC 253 XMM2	$0.18^{+0.17}_{-0.08}$	$1.10^{+0.42}_{-0.55}$	$1.32^{+1.90}_{-1.32}$	$6.82^{+4.19}_{-2.22}$	$1.27^{+0.71}_{-0.40}$	$2.15^{+0.84}_{-0.58}$	0.93	20651
NGC 5204 XMM1	$0.18^{+0.05}_{-0.04}$	$1.00^{+0.30}_{-0.40}$	$0.0^{+0.59}_{-0.0}$	$3.21^{+0.98}_{-0.95}$	$6.86^{+0.67}_{-0.09}$	$3.28^{+0.39}_{-0.38}$	0.95	16717
	$0.20^{+0.06}_{-0.05}$	$0.63^{+0.35}_{-0.48}$	$0.0^{+0.62}_{-0.0}$	$2.95^{+2.13}_{-1.84}$	$7.37^{+1.35}_{-2.08}$	$3.16^{+0.50}_{-0.44}$	0.94	13864
NGC 300 XMM1	$0.21^{+0.05}_{-0.03}$	$1.59^{+0.22}_{-0.26}$	$0.0^{+0.53}_{-0.0}$	$1.69^{+0.85}_{-0.32}$	$0.73^{+0.18}_{-0.13}$	$3.89^{+0.21}_{-0.32}$	1.00	11479
N4559 X-7	$0.20^{+0.06}_{-0.05}$	$0.34^{+0.38}_{-0.34}$	$0.0^{+0.48}_{-0.0}$	$5.79^{+2.82}_{-2.75}$	$6.63^{+1.44}_{-2.42}$	$3.13^{+0.55}_{-0.50}$	0.83	12506
NGC 5408 X-1	$0.18^{+0.05}_{-0.04}$	$0.87^{+0.28}_{-0.42}$	$0.45^{+1.75}_{-0.45}$	$2.29^{+1.57}_{-1.28}$	$4.87^{+1.23}_{-1.02}$	$4.09^{+0.28}_{-0.34}$	0.89	10045

^a Hydrogen column density determined from `tbvarabs`. The Galactic value of n_{H} was fixed to the Dickey & Lockman (1990) value with the `tbabs` model.

^b Element abundance relative to the Wilms solar abundance from the `tbvarabs` model.

^c Ratio of mass accretion rate from the `grad` model to Eddington accretion rate (see § 4).

^d Total number of photon counts from pn and MOS detectors.

for NGC 4631 XMM1, with an estimated mass of $5.5 M_{\odot}$ and an accretion rate L/L_{Edd} of 0.84, are also consistent with the standard high-state Galactic black hole model. This source is likely a normal stellar mass black hole X-ray binary in an external galaxy.

The remaining sources with $M_{\text{grad}} \ll 100 M_{\odot}$ (M33 X-8, M81 XMM1, NGC 4559 X-10, and M83 XMM1) yielded L/L_{Edd} ratios in the range of 1–3. These sources are also those described in the previous section where the power-law component fits the low-energy spectrum. They are also well fitted by a Comptonization model and correspond to a subclass of high-luminosity ULXs de-

scribed in Paper I. Due to the luminosity and modeled disk temperature ($kT \approx 1 \text{ keV}$), we suggested that these sources were very high state stellar mass black hole systems. In order to be consistent with the black hole accretion model assumed in this study, the spectra of these sources should be the result of Comptonization from a thermal disk spectrum.

To test this further, we fitted the spectrum of the highest count source of this type (M33 X-8) with an absorbed thermal disk and Comptonization model [`tbabs*tbabs*(diskpn+comptt)`]. The `comptt` model has the following parameters: a seed temperature (keV), a plasma temperature (keV), and optical depth of the medium. We used the `diskpn` model in place of the `grad` model since the former provides a disk temperature to which the `comptt` seed temperature can be fixed. This provides a physical model, where the thermal disk supplies the energy for the Compton tail. M33 X-8 was well fitted by this model with a $\Delta\chi^2/\text{dof} = 1659.9/1534$ (1.08). Thus, these sources are still consistent with the black hole accretion model. Replacing the `tbabs` model used for the galactic column density with the `tbvarabs`, we measured the column density, oxygen abundance, and iron abundance. With this thermal disk and Comptonization model we obtained $n_{\text{H}} = 1.5^{+0.04}_{-0.08} \times 10^{21} \text{ cm}^{-2}$, $\text{O}/\text{H} = 1.26^{+0.08}_{-0.15}$, and $\text{Fe}/\text{H} = 2.83^{+0.71}_{-0.76}$, with a $\Delta\chi^2/\text{dof} = 1577.3/1534$ (1.03). Within the error bars, these results are consistent with those seen in Table 2.

5. PROPERTIES OF THE ISM IN ULX HOST GALAXIES

The major question to be examined in using ULXs as probes of the ISM is whether the hydrogen column density and element abundances are primarily from the host galaxy or intrinsic to the local environment of the ULX. Before we can answer this question, it is important to understand the intrinsic spectrum of the source. In the previous section we discussed the nature of the soft component in light of the high-S/N spectra of the 14 ULXs we examined. We found that if the spectrum is due to thermal emission from a disk, modeling the spectrum with a variety of disk models (`grad`, `diskbb`, `diskpn`, `bbody`) does not significantly change the measured oxygen abundance or hydrogen column density.

Assuming the reliability of the hydrogen column density and abundance measurements, based on their model-independent values, we investigate the source of the absorption in ULX spectra. In order to determine whether the model n_{H} values suggest the necessity of extra local absorption, we compare the model values with column densities obtained from H I studies. We investigate this in § 5.1. The oxygen abundances (as an indication of

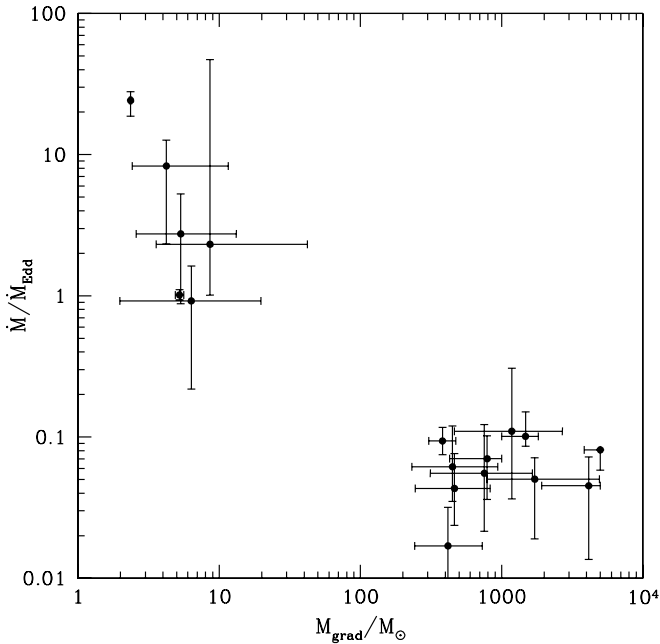


FIG. 4.—Black hole mass vs. mass accretion rate (per Eddington accretion rate) obtained from the general relativistic disk model (`grad`). The sources with model parameters indicating high masses correspond to accretion rates that are below 40% of the Eddington accretion rate for the given mass. In Paper I we noted a temperature gap in the range of 0.26–0.50 keV from spectral fits utilizing an absorbed blackbody and power-law model. In this figure we see that there is a gap in mass from the parameters of the absorbed general relativistic disk and power-law model. The values shown are results for the EPIC spectra only, as recorded in Table 2 (for all sources in Table 2). Therefore, there are multiple points for the sources with multiple observations. We plotted these sources (Holmberg II XMM1, Holmberg IX XMM1, M81 XMM1, and NGC 5204 XMM1) twice to confirm that their masses, as determined by the `grad` model, do not vary.

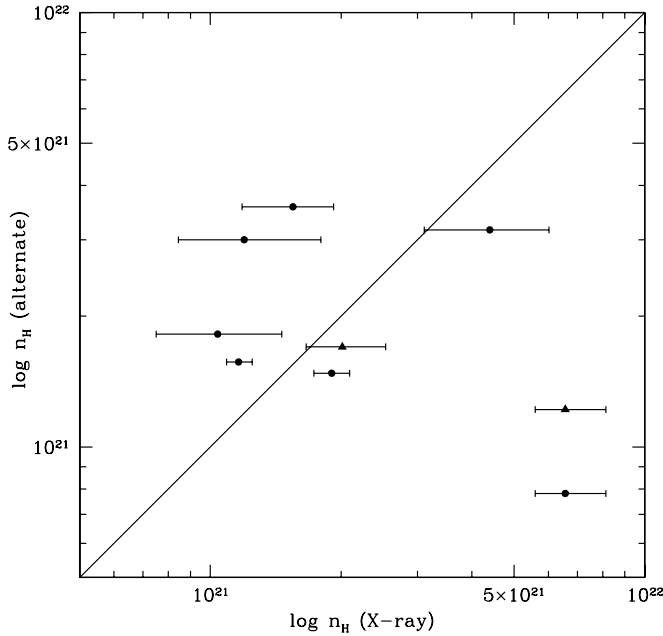


FIG. 5.—Hydrogen column density from E_{B-V} (triangles) or H I studies (circles) vs. the hydrogen column density obtained from the *tbvarabs* model. H I column densities were obtained for Holmberg II, NGC 5204, and NGC 4559 through the WHISP survey (Swaters et al. 2002). Additional H I column densities were obtained for NGC 247, Holmberg IX, and M81 through VLA data (Braun 1995). The X-ray spectral fit columns are not biased toward significantly higher values than the alternate method column densities. This implies that most of the matter in the line of sight is from H I. This is not true, however, for the source M81 XMM1 (represented by the two outlying points in the lower left portion of the graph) where the X-ray column density is much greater than those from the optical and radio.

metallicity), which we examine in § 5.2, can provide further clues of whether the absorption we see in the X-ray spectrum is intrinsic to the source. We also examine possible connections between the host galaxy’s star formation rate and elemental abundances.

5.1. Column Densities

To determine whether the ULX X-ray hydrogen column densities represent largely galactic column densities or column densities local to the ULX, we compared the X-ray values to those obtained from optical and radio studies. For a comparison to hydrogen column densities from optical studies, we used interstellar reddening values. In a study of dust scattering X-ray halos surrounding point sources and supernova remnants, Predehl & Schmitt (1995) derived a relationship between hydrogen column density and interstellar reddening, using X-ray data. They found that $n_H = 5.3 \times 10^{21} \text{ cm}^{-2} E_{B-V}$. They also found that these X-ray-derived column densities are not affected by the intrinsic absorption of the X-ray source. Thus, the optical reddening, E_{B-V} , becomes a useful tool in checking our own X-ray-derived column densities. Through a literature search, we found E_{B-V} values for the sources M33 X-8 (0.22; Long et al. 2002) and M81 XMM1 (0.23; Kong et al. 2000). The corresponding E_{B-V} -derived n_H values are plotted in Figure 5 as triangles.

For a comparison of X-ray-derived hydrogen column densities with radio values, we obtained H I column densities for four objects (Holmberg II XMM1, NGC 4559 X-7, NGC 4559 X-10, and NGC 5204 XMM1) from the WHISP catalog (Swaters et al. 2002). These are radio H I column densities within the host galaxy (galactic), not the Galactic columns. Exact values of the H I column densities were computed and given to us by Rob Swaters. In addition, we include H I column densities of NGC 247 XMM1,

TABLE 6
COLUMN DENSITIES FROM OPTICAL AND H I STUDIES

Source	n_H^a (10^{22} cm^{-2})	Method ^b
NGC 247 XMM1	0.316	H I
M33 X-8	0.170	E_{B-V}
Holm II XMM1	0.157	H I
M81 XMM1	0.122	E_{B-V}
M81 XMM1	0.078	H I
Holm IX XMM1	0.148	H I
NGC 4559 X-7	0.357	H I
NGC 4559 X-10	0.300	H I
NGC 5204 XMM1	0.182	H I

^a Hydrogen column density (galactic, not Milky Way) determined by the method indicated.

^b Column densities computed from reddening values (E_{B-V}) or from radio H I measurements; see § 5.1 for details.

M81 XMM1, and Holmberg IX XMM1 from Braun (1995). We obtained the FITS files of H I column density maps from this paper (available on NED), where the pixel value corresponds to the galactic column density in units of 10^{18} cm^{-2} . The H I n_H values from both studies are plotted in Figure 5 as circles. The column densities, from the radio and reddening studies, are listed in Table 6.

We find that the host galaxy column densities from alternate methods (optical or radio studies) are not significantly different from the X-ray column densities. Particularly, the X-ray values are not skewed toward substantially higher values than the optical/radio values. Thus, the X-ray columns are likely the galactic values without any additional local absorption. The exception, however, is M81 XMM1 (represented by two points in Figure 5, one for each of the methods). The E_{B-V} value ($1.22 \times 10^{21} \text{ cm}^{-2}$) and the H I value ($0.78 \times 10^{21} \text{ cm}^{-2}$) are significantly lower than the X-ray column density. This may indicate the presence of extra absorption around this source.

The result that the X-ray hydrogen column densities are in good agreement with those from H I studies and interstellar extinction values is interesting considering that the X-ray-measured column densities are along a direct line of sight to the ULXs while the H I measurements are an average over a larger beam area. The agreement between the two measurements implies that the ULXs, with the exception of M81 XMM1, lie within roughly normal areas of their host galaxies (i.e., not in regions of higher column density such as a molecular cloud).

5.2. Elemental Abundances

5.2.1. Test for Oxygen Ionization Level

Before discussing implications of the determined oxygen and iron abundances, we relate a test performed to determine whether we could distinguish between different ionization levels of oxygen. To do this, we used the absorption edge model, *edge*, in XSPEC [using the full model: *tbabs*tbvarabs*edge*edge*(grad+pow)*]. We first checked to see that the abundance values obtained with the *edge* model matched the values from the *tbvarabs* model. We fixed the oxygen abundance in the *tbvarabs* model at zero and added the *edge* model, allowing the threshold energy and absorption depth (τ) to float as free parameters (with an initial energy set to 0.543 keV). We fitted this model to the longest observations of Holmberg II XMM1 and Holmberg IX XMM1 in addition to a source with a lower number of counts, NGC 5408 XMM1 (0112290601).

TABLE 7
SPECTRAL FITS FOR OXYGEN EDGE WITH THE `tbabs*tbvarabs*edge*edge*(grad+pow)` MODEL

Source	n_{H}^{a} (10^{22} cm^{-2})	E^{b}	τ^{c}	n_{O}^{d} (10^{17} cm^{-2})	[O/H] ^e	χ^2/dof	Counts ^f
Holm II XMM1	$0.16^{+0.01}_{-0.01}$	$0.566^{+0.01}_{-0.01}$	$0.35^{+0.02}_{-0.01}$	7.2	8.65/8.64	2543/2017	342874
Holm IX XMM1	$0.19^{+0.02}_{-0.02}$	$0.543^{+0.01}_{-0.01}$	$0.62^{+0.11}_{-0.12}$	12.0	8.81/8.82	2887/2751	148061
NGC 5408 XMM1	$0.17^{+0.06}_{-0.03}$	$0.538^{+0.04}_{-0.02}$	$0.37^{+0.29}_{-0.21}$	7.1	8.61/8.63	298/334	10045

^a Hydrogen column density determined from `tbvarabs`. The Galactic value of n_{H} was fixed to the Dickey & Lockman (1990) value with the `tbabs` model.

^b Threshold energy obtained from the `edge` model in keV. Note that one `edge` model was used to correct for the difference in the oxygen edge between the pn, MOS1, and MOS2 CCDs. The other `edge` model was used to measure the oxygen abundance from the 542 eV K-shell edge.

^c Absorption depth obtained from the `edge` model.

^d Column density of oxygen estimated from the `edge` model.

^e Abundance of oxygen relative to hydrogen from the `edge` model vs. the value quoted in Table 2, $[\text{O}/\text{H}] = 12 + \log(\text{O}/\text{H})$, where O is oxygen abundance and H is hydrogen abundance.

^f Total number of photon counts from the pn and MOS detectors.

To find the oxygen column density (n_{O}), we used the relationship that $\tau = \sigma n_{\text{O}}$, where σ is the cross section for photoabsorption. We used the cross section values for neutral oxygen published in Reilman & Manson (1979) as an estimate. This choice is supported by the results of Juett et al. (2004), who measured the ratio of oxygen ionization states in the ISM as $\text{O II}/\text{O I} \approx 0.1$. In Table 7, the hydrogen column density, threshold energy, and optical depth are listed for the sources fitted with this model. From Reilman & Manson (1979) we used the cross section values of $\sigma = 5.158 \times 10^{-19} \text{ cm}^2$ (for $E = 0.540 \text{ keV}$) and $\sigma = 4.789 \times 10^{-19} \text{ cm}^2$ (for $E = 0.570 \text{ keV}$). As seen in Table 7, the hydrogen column densities and the oxygen abundances obtained from this model are close to those from the `tbvarabs` model. The [O/H] values, where $[\text{O}/\text{H}] = 12 + \log(\text{O}/\text{H})$ and O and H represent oxygen column density and hydrogen column density, respectively, between the two models vary by less than 1%.

To test whether the threshold energy from the `edge` model is affected by the ionization level of oxygen, we simulated spectra of an absorbed power-law model with an oxygen edge. Tim Kallmann (P.C.) provided us with an oxygen edge model incorporating the cross sections of Garcia et al. (2005). The model allows for a variation of the ratio of $\text{O II}/\text{O I}$. Using the response and ancillary response matrices from the long Holmberg II ULX observation, we simulated spectra with the XSPEC `fakeit` command for a $\Gamma = 2.35$ power law. We simulated spectra for $\text{O II}/\text{O I}$ ratios of 0.0, 0.2, 0.4, 0.6, 0.8, and 1.0. The simulated spectra were binned with a minimum of 20 counts bin^{-1} . The absorption edge component of the spectrum was then fitted with the `edge` model. The fits to the threshold energies for the simulated spectra yielded values ranging from 0.53 to 0.59 keV, with no preference of lower $\text{O II}/\text{O I}$ ratios corresponding to lower threshold energies. Since the O I absorption edge occurs at $E = 0.543 \text{ keV}$ and the O II absorption edge occurs at $E = 0.57 \text{ keV}$, we could not distinguish between these ionization states of oxygen. Our simulations show that the oxygen edge measurements will be sensitive to O I and O II but not to high ionization states (for instance, O VIII , which has an edge energy of 0.87 keV).

5.2.2. X-Ray/Optical [O/H] Comparison

As noted above, we tested the oxygen abundances obtained with the absorption model `tbvarabs` against the abundances obtained from adding a photoelectric absorption edge model, for three of the ULXs. We found good agreement ($< 1\%$ difference in [O/H] values) between both models for the X-ray spectra. However, we found that it is not possible to distinguish between different low ionization states of oxygen using the `edge` model.

We now discuss comparisons of our X-ray oxygen absorption values with measurements in different wavelengths, based on a literature search for [O/H] ratios. In Figure 6 we compare our [O/H] ratios with those of a study conducted by Pilyugin et al. (2004) (*circles*). They provide a compilation of [O/H] ratios determined through spectrophotometric studies of H II regions. Their [O/H] values are based on the radial distribution of oxygen abundance using the P method. They determined [O/H] values for spiral galaxies where published spectra were available for at least four H II regions. In addition, they reference [O/H] values for irregular galaxies obtained through alternate methods. Our [O/H] values are determined from the oxygen abundances listed in Table 2. Thus, $[\text{O}/\text{H}] = 12 + \log(\text{O} \times 0.00049)$. O is the oxygen abundance obtained from the model, which is multiplied by

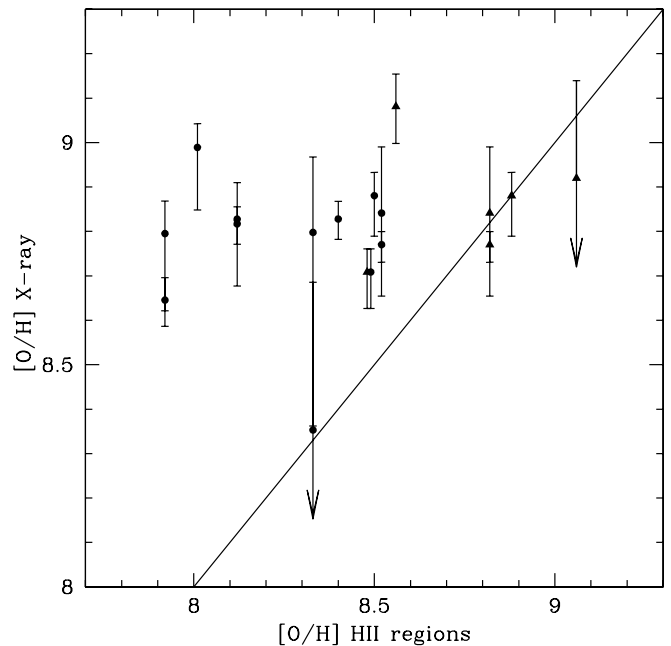


FIG. 6.—Oxygen abundances from studies of H II regions vs. oxygen abundances from the `tbvarabs` model. The [O/H] ratios are given for Holmberg II XMM1, NGC 5408 XMM1, Holmberg IX XMM1, NGC 4559 XMM1, NGC 4559 XMM2, NGC 1313 XMM3, M33 X-8, NGC 300 XMM1, NGC 253 XMM2, and M81 XMM1 using the P calibration method (*circles*). Also, [O/H] ratios are included for M33 X-8, NGC 300 XMM1, M81 XMM1, NGC 253 XMM2, and M83 XMM1 using the R_{23} calibration method (*triangles*). Arrows indicate that the lower limit for the [O/H] X-ray parameter is below the plotted graph region. Our values are high compared to the P method but in good agreement with the R_{23} method. The sources with the largest difference between [O/H] values are those located in irregular galaxies.

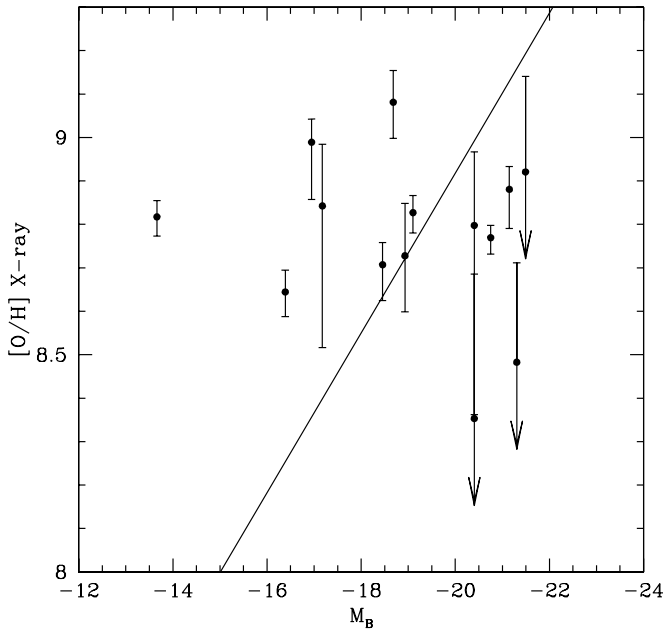


FIG. 7.—Host galaxy M_B vs. ULX X-ray $[O/H]$ ratio. The solid line represents the SDSS results from a study of star-forming galaxies (Tremonti et al. 2004). Arrows indicate that the lower limit for the $[O/H]$ X-ray parameter is below the plotted graph region. Our values are largely consistent with the SDSS results, with the exception of Holmberg IX and Holmberg II. Both of these galaxies are irregulars. The X-ray $[O/H]$ ratio derived from the ULX spectra is higher than predicted for these objects.

the Wilms relative abundance of 4.9×10^{-4} of oxygen to hydrogen. We were able to compare $[O/H]$ values for the sources located in M33, NGC 253, NGC 300, M81, Holmberg II, NGC 4559, and NGC 5408. We include the $[O/H]$ value computed for the Holmberg IX ULX by Miller (1995) of 8.12. This value was computed from an optical study of the surrounding H II region. Also, we add the $[O/H]$ value of 8.4 for NGC 1313, determined separately by both Calzetti & Kinney (1994) and Walsh & Roy (1997).

As shown in Figure 6, our $[O/H]$ values are consistently high compared to those obtained from the Pilyugin et al. (2004) H II study. Pilyugin et al. (2004) include a discussion of how their values, obtained by the P calibration method, are significantly lower than those obtained by Garnett (2002) using the R_{23} calibration method. In Figure 6 we include $[O/H]$ values for NGC 253, NGC 300, M33, M81, and M83 from Garnett (2002) (triangles). Our oxygen abundances are in much better agreement with the values from this R_{23} calibration method.

Our $[O/H]$ values, which are consistent in the X-ray band between two separate absorption models [tbabs*tbvarabs*edge*(grad+pow) and a tbabs*edge*edge*(grad+pow) model], are consistent with the values of Garnett (2002). We further wish to compare them to the metallicity predicted from Sloan Digital Sky Survey (SDSS) results. As a result of an SDSS study, Tremonti et al. (2004) found a luminosity-metallicity relation for their sample of star-forming galaxies of $12 + \log(O/H) = -0.185 (\pm 0.001)M_B + 5.238 (\pm 0.018)$. In Figure 7 we compare our values with their results (represented by the line). We obtained absolute magnitudes (M_B) for the host galaxies using the total apparent corrected B magnitude recorded in the HyperLeda galaxy catalog (Paturel et al. 1989) (parameter *btc*) and the distances listed in Table 1 of Paper I. For M33 and NGC 4559, which were not included in the previous study, we used the distances of 0.7 and 9.7 Mpc from Ho et al. (1997). The majority of our sources are consistent with the SDSS results. However, the sources in irregular galaxies have metallicities much higher than predicted.

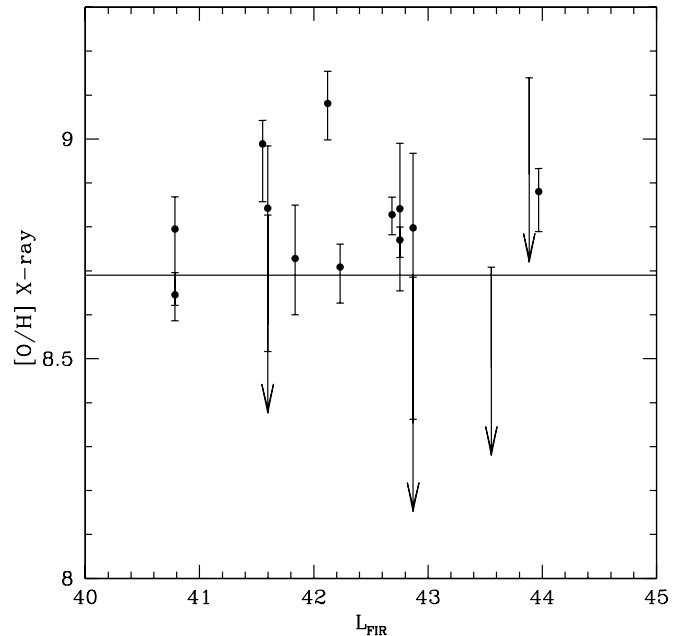


FIG. 8.—Oxygen abundance ($[O/H]$) as a function of the host galaxy's FIR luminosity, obtained from *IRAS*. The line represents the Wilms solar value of $[O/H]$. Arrows indicate that the lower limit for the $[O/H]$ X-ray parameter is below the plotted graph region. There appears to be no correlation between L_{FIR} and oxygen abundance. In fact, the sources show roughly solar $[O/H]$ abundances regardless of host galaxy.

5.2.3. Galaxy Properties

More luminous galaxies are sometimes expected to have higher star formation rates and thus higher metallicity. However, we found no evidence of this. Investigating further into the relationship between star formation rate (SFR) and metallicity, we chose to look at a galactic luminosity diagnostic that is less dependent on extinction from dust, the infrared galactic luminosity (L_{FIR}). In Paper I we calculated L_{FIR} using data from the *Infrared Astronomical Satellite (IRAS)* and the approach of Swartz et al. (2004). We quoted values of L_{FIR} in Paper I. Using the same method, with *IRAS* fluxes obtained from Ho et al. (1997), we find M33 to have $L_{FIR} \approx 1.7 \times 10^{42}$ ergs s^{-1} and NGC 4559 to have $L_{FIR} \approx 7.4 \times 10^{42}$ ergs s^{-1} . We used these L_{FIR} values to compare the SFR to both the oxygen and iron abundances.

In Figure 8 we plot oxygen abundance relative to SFR. All sources with the exception of Holmberg IX XMM1, which did not have available *IRAS* data, are plotted. We see, as was also illustrated in Figure 7, that the luminosity of the host galaxy does not determine the metallicity. The more luminous galaxies do not have metallicities higher than the less luminous galaxies. In fact, most sources have oxygen abundances that are roughly the Wilms solar abundances (indicated by the line).

In Figure 9 we see that there is no relationship between iron abundance (see values in Tables 2 and 3 for values) and SFR. The Wilms solar abundance for iron is only 2.69×10^{-5} relative to the hydrogen abundance. The plots show that the metallicity relationship is very flat, and all of the sources have roughly solar abundances. This is also seen in Figure 10. This plot shows the $[Fe/H]$ ratios versus the $[O/H]$ values, both obtained through the tbvarabs model. The solar Wilms values are represented on the plot by the open circle. It appears that the sources are slightly more abundant in iron than the solar value; however, the error bars are quite large. The oxygen abundances, as before stated, are roughly the solar Wilms value. Roughly, the abundances appear solar.

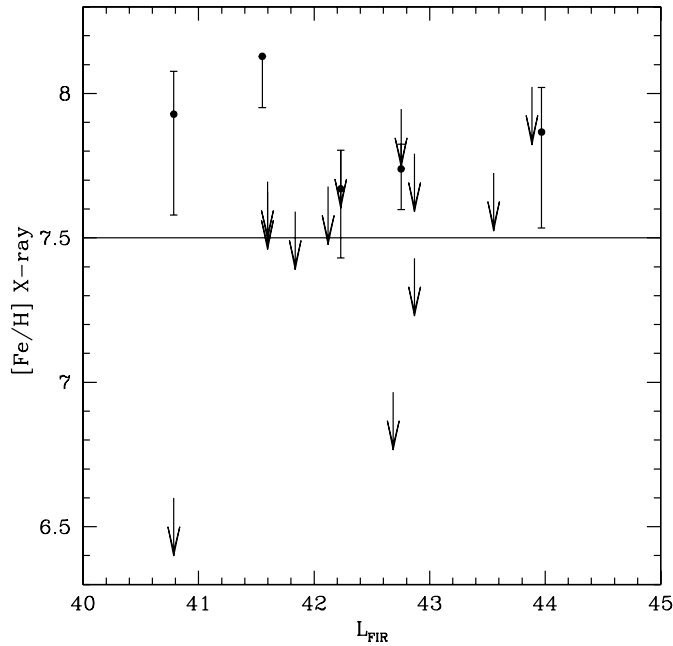


FIG. 9.—Iron abundance ($[\text{Fe}/\text{H}]$) as a function of the host galaxy's FIR luminosity obtained from *IRAS*. Holm IX did not have corresponding IR data; however, being an irregular galaxy, its L_{FIR} would probably be comparable to Holm II. The iron abundances of both of the irregular galaxies are well above those of the ULXs in spiral galaxies. The sources in galaxies with larger L_{FIR} have roughly equal iron abundances, within the error bars. The iron abundances in all cases are well above the Wilms solar abundance. Arrows indicate that the lower limit for the $[\text{Fe}/\text{H}]$ X-ray parameter is below the plotted graph region.

With such a flat relationship between abundance and luminosity, we tested to see if this result carried through in a comparison of abundance versus radial distance within the host galaxy. This follows on an interesting property observed in spiral galaxies, namely, that abundances are typically higher in the center of the

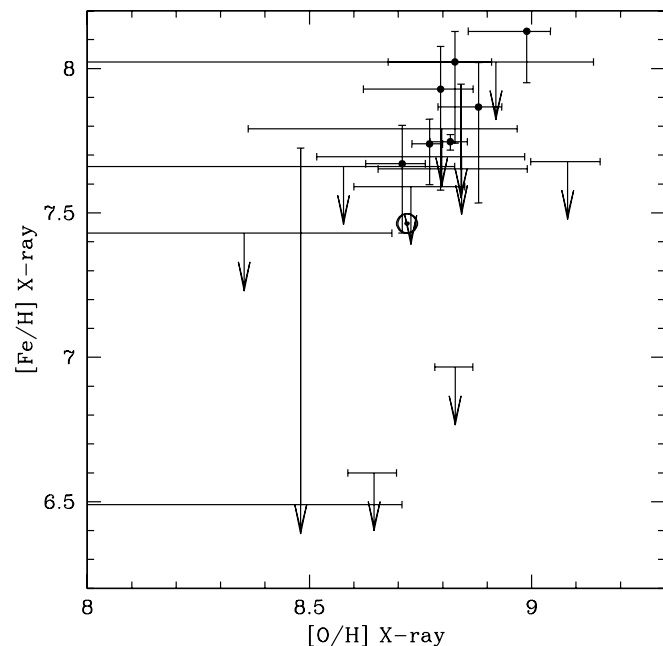


FIG. 10.— $[\text{Fe}/\text{H}]$ as a function of $[\text{O}/\text{H}]$ from the *tbvarabs* model, using the *grad* and power-law fit. The Wilms solar abundance is indicated with an open circle. The ratios of Fe/O abundances obtained through the X-ray spectral fits are approximately the Wilms solar values. Arrows indicate that the lower limit for the $[\text{Fe}/\text{H}]$ X-ray parameter is below the plotted graph region.

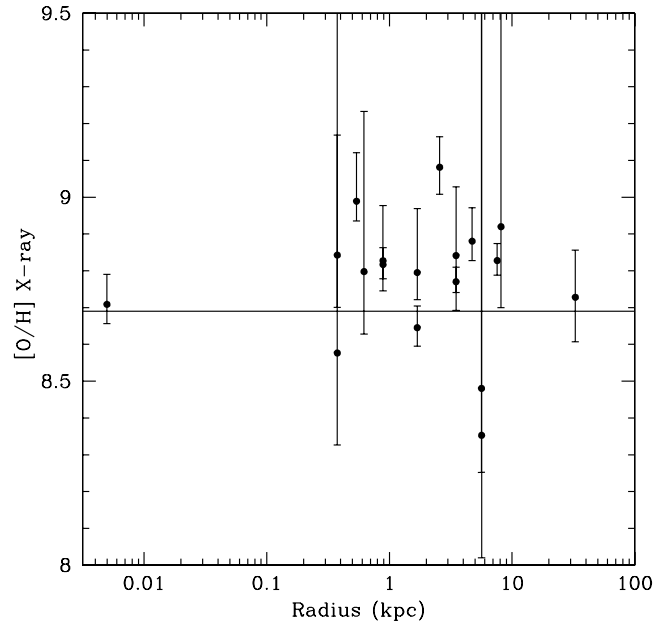


FIG. 11.—Oxygen abundances from the *tbvarabs* model vs. distance of the ULX from the host galaxy's dynamical center. The $[\text{O}/\text{H}]$ ratios are given for spiral galaxies only. There is no correlation between radius and oxygen abundance in our sample. However, since the sources originate in different host galaxies with different abundances, there is no conclusion that can be drawn from these data. The host galaxy NGC 4559, containing two ULXs studied, does appear to show a possible correlation (the source nearer the center has a higher oxygen abundance); however, the error bars on the oxygen abundance are large for both sources.

galaxy and decrease with increasing radius (Searle 1971). We tested how our results compare to this result in Figure 11. For the sources located within spiral galaxies, we plotted the $[\text{O}/\text{H}]$ ratio as a function of distance R from the dynamical center (as reported by NED). We used the distances quoted in Table 1 of Paper I to translate angular distance on the sky into kiloparsecs from the galactic center. As evidenced in the plot, we do not see much variation in the $[\text{O}/\text{H}]$ values. Clearly, the expected scaling of higher oxygen abundance toward the center is not seen. Since the sources lie in different host galaxies with different relative abundances, it is possible that this trend may be detectable with a larger sample of galaxies. However, the implication from Figures 7–11 is that the environment of the ULXs is relatively uniform in terms of metallicity. The ULXs appear to live in similar environments, with metallicities roughly solar.

6. SUMMARY

Through our work, we conclude that X-ray spectral fits to ULXs do provide a viable method of finding abundances in other galaxies. We have determined hydrogen column densities and oxygen abundances along the line of sight to 14 ULXs. To measure these values, we assumed a connection between ULXs and Galactic black hole systems such that the ULX spectra used in this study correspond to a high/soft state. Therefore, we modeled the sources with an absorbed disk model and power law [in XSPEC `tbabs*tbvarabs*(accretion disk model+ pow)`]. We tested the effect different accretion disk models have on the measurement of the host galaxy's hydrogen column density and elemental abundance with the disk models: *grad*, *diskpn*, *diskbb*, and *bbody*. We found that the measured hydrogen column density and abundances are model independent.

We also tested the physical plausibility of this model by comparing the mass and mass accretion rates obtained from the *grad* model with expected results based on Galactic black hole systems. We

found that the ULX spectra were consistent with the high/soft state, with L/L_{Edd} values < 1.0 for sources with a standard thermal model at low energies and power-law-dominated higher energy spectrum. For four sources, the spectra were consistent with a heavily Comptonized spectrum. These sources are more likely stellar mass black hole systems in a very high state of accretion. We modeled their spectra with a power law at low energy and disk model around 1 keV. This model provided similar column density and abundance values to a more physical absorbed disk and Comptonization model.

Comparing our X-ray-measured column densities with those from optical and H I studies for eight of our sources, we find that seven of the sources have X-ray column densities approximately equal to those of the alternate methods. This implies that the hydrogen columns toward most of our ULXs represent that of their host galaxy. Since the H I studies represent averages over a large beam area where the X-ray column densities are directly along the line of sight to the ULX, this implies that the ULXs lie within roughly normal areas of their host galaxies. The exception in this study was M81 XMM1, whose X-ray hydrogen column density was large relative to the H I study. This suggests that there is extra absorption intrinsic to this source.

The oxygen abundances appear to be roughly the Wilms solar values. For five sources, the count rates were sufficient to determine iron abundances without large error bars (see Figs. 9 and

10). We found that iron abundances for these sources were slightly overabundant relative to the solar Wilms value. However, within error bars, the abundances appear solar. X-ray-derived [O/H] values are comparable to those from an optical study by Garnett (2002), indicating that the X-ray-derived values are the same as the [O/H] values of H II regions within the host galaxy. Luminosity-metallicity relationships for the ULX host galaxies show a flat distribution, as does a radius-metallicity plot. Therefore, it appears that the ULXs exist in similar environments within their host galaxy, despite the wide range of host galaxy properties.

We would like to thank Rob Swaters and Robert Braun for help with the H I column densities and Tod Strohmayer for use of the 100 ks Holmberg IX *XMM-Newton* data set before it became public. We would also like to thank Tim Kallmann for useful discussion on the oxygen absorption edge and an anonymous referee for suggestions which greatly improved this paper. This research has made use of the NASA/IPAC Extragalactic Database (NED), which is operated by the Jet Propulsion Laboratory, California Institute of Technology, under contract with the National Aeronautics and Space Administration as well as the HyperLeda database located online at <http://leda.univ-lyon1.fr/>.

APPENDIX A

SPECTRAL SIMULATIONS

We conducted spectral simulations in order to (1) determine the number of counts needed to measure the oxygen and iron abundances and (2) to verify the model independence of the galactic column density and abundances with respect to the *grad*, *diskbb*, and *bbody* models (seen in a comparison of Tables 2 and 4). Toward this end, we created simulated pn spectra based on the long Holmberg IX XMM1

TABLE 8
SPECTRAL FITS TO SIMULATED HOLM IX XMM1 *tbabs***tbabs**(*grad*+*pow*) SPECTRUM

Counts ^a	n_{H}^{b} (10^{22} cm^{-2})	Oxygen Abundance ^c	Iron Abundance ^c	χ^2/dof
<i>tbabs</i> * <i>tbvarabs</i> *(<i>grad</i> + <i>pow</i>)				
200000.....	0.21 ^{+0.02} _{-0.02}	1.08 ^{+0.13} _{-0.15}	0.87 ^{+0.68} _{-0.76}	1687/1727
40000.....	0.19 ^{+0.04} _{-0.03}	1.15 ^{+0.26} _{-0.33}	0.97 ^{+1.41} _{-0.97}	933/914
10000.....	0.20 ^{+0.07} _{-0.06}	1.55 ^{+0.41} _{-0.52}	0.90 ^{+2.64} _{-0.90}	340.5/401
5000.....	0.16 ^{+0.13} _{-0.07}	1.37 ^{+0.75} _{-1.34}	1.36 ^{+3.64} _{-1.36}	187.2/201
2000.....	0.33 ^{+0.14} _{-0.19}	1.20 ^{+0.57} _{-1.20}	5.0 ^{+0.0} _{-5.0}	71.9/89
<i>tbabs</i> * <i>tbvarabs</i> *(<i>diskbb</i> + <i>pow</i>)				
200000.....	0.21 ^{+0.02} _{-0.02}	1.09 ^{+0.15} _{-0.19}	0.99 ^{+0.94} _{-0.76}	1691/1727
40000.....	0.19 ^{+0.03} _{-0.03}	1.16 ^{+0.27} _{-0.35}	1.09 ^{+1.47} _{-1.09}	934/914
10000.....	0.19 ^{+0.03} _{-0.05}	1.58 ^{+0.43} _{-0.50}	1.01 ^{+2.80} _{-1.01}	341/401
5000.....	0.16 ^{+0.12} _{-0.08}	1.41 ^{+0.76} _{-1.16}	1.57 ^{+3.43} _{-1.57}	187.5/201
2000.....	0.32 ^{+0.18} _{-0.19}	1.23 ^{+0.59} _{-1.23}	5.0 ^{+0.0} _{-5.0}	71.7/89
<i>tbabs</i> * <i>tbvarabs</i> *(<i>bbody</i> + <i>pow</i>)				
200000.....	0.17 ^{+0.02} _{-0.02}	1.24 ^{+0.16} _{-0.20}	1.65 ^{+0.85} _{-1.01}	1702/1727
40000.....	0.15 ^{+0.04} _{-0.02}	1.28 ^{+0.36} _{-0.40}	1.73 ^{+1.97} _{-1.72}	937/914
10000.....	0.15 ^{+0.07} _{-0.04}	1.77 ^{+0.61} _{-0.72}	1.22 ^{+3.78} _{-1.22}	343.7/401
5000.....	0.13 ^{+0.10} _{-0.07}	1.61 ^{+0.97} _{-1.61}	2.19 ^{+2.81} _{-2.19}	187.5/201
2000.....	0.21 ^{+0.19} _{-0.12}	1.16 ^{+0.92} _{-1.16}	5.0 ^{+0.0} _{-5.0}	71.8/89

^a Total number of photon counts for simulated pn spectrum. Simulated spectra created with the XSPEC *fakeit* command, using the model parameters and response files from the long Holm IX XMM1 observation.

^b Hydrogen column density determined from *tbvarabs*. The Galactic value of n_{H} was fixed to the Dickey & Lockman (1990) value with the *tbabs* model.

^c Element abundance relative to the Wilms solar abundance from the *tbvarabs* model.

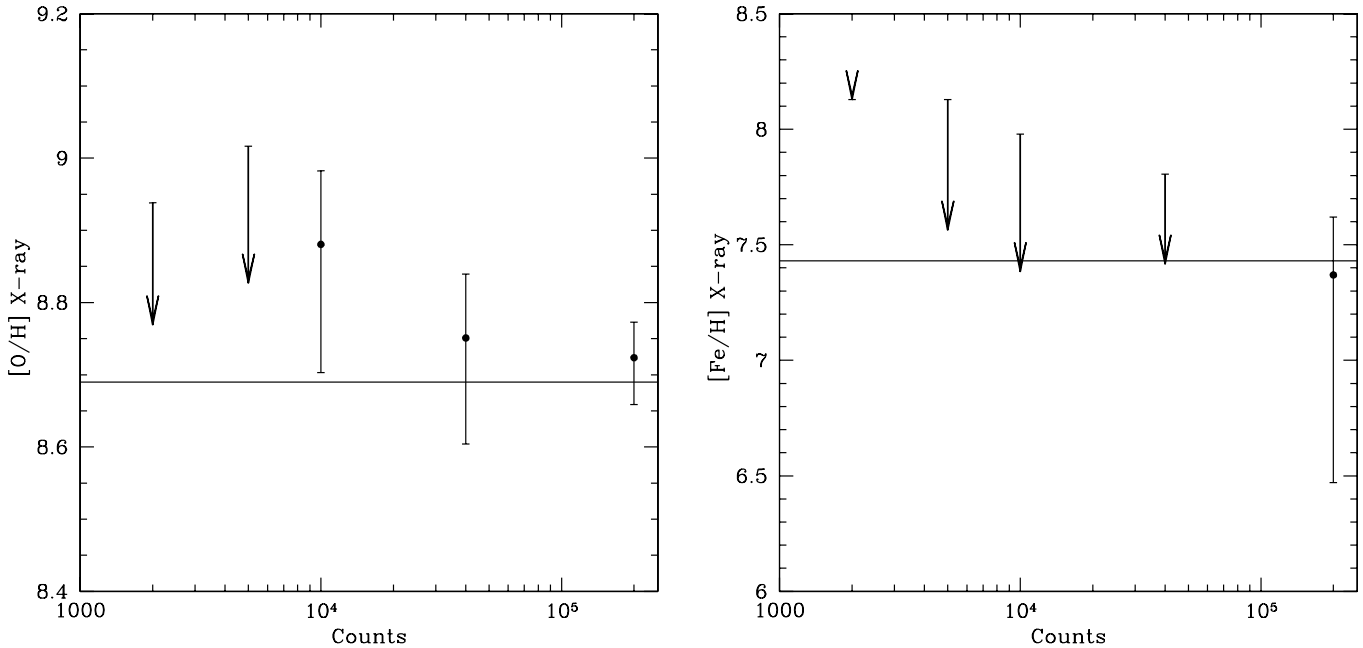


Fig. 12.—Number of counts for simulated spectra vs. the $[O/H]$ value (*left*) and $[Fe/H]$ value (*right*) from the $\text{tbabs}^*\text{tbvarabs}^*(\text{grad}+\text{pow})$, where errors represent the 90% confidence rate. The horizontal lines represent the solar Wilms values ($[O/H] \approx 8.69$ and $[Fe/H] \approx 7.43$). Arrows are used to represent errors that extend below the range of the plot. The tip of the arrow point represents the $[O/H]$ or $[Fe/H]$ parameter from the XSPEC model (see Table 8).

observation's (0200980101) unbinned, pn spectrum. We used the base ($\text{grad}+\text{pow}$) model parameters as indicated in Table 2. We modeled both the Galactic column density (Dickey & Lockman [1990] value: $n_{\text{H}} = 4.0 \times 10^{20} \text{ cm}^{-2}$) and host galaxy column density ($n_{\text{H}} = 1.9 \times 10^{21} \text{ cm}^{-2}$) with individual tbabs models. Thus, all of the abundances were set to the solar Wilms values. We used the XSPEC command `fakeit` to create simulated spectra with 200,000, 40,000, 10,000, 5000, and 2000 counts. The simulated spectra were binned with 20 counts bin^{-1} using `grppha`. We fitted the binned simulated spectra with the models $\text{tbabs}^*\text{tbvarabs}^*(\text{grad}+\text{pow})$, $\text{tbabs}^*\text{tbvarabs}^*(\text{diskbb}+\text{pow})$, and $\text{tbabs}^*\text{tbvarabs}^*(\text{bbody}+\text{pow})$. This allowed us to see the effects the different models have on the measured galactic hydrogen column density and abundances. The results for these fits are seen in Table 8. The range that the oxygen and iron abundances were allowed to vary within was from 0.0 (lower limit) to 5.0 (upper limit) with respect to the solar values.

In Figure 12, the number of simulated counts versus the errors on the oxygen and iron abundances are plotted for the $\text{tbabs}^*\text{tbvarabs}^*(\text{grad}+\text{pow})$ model. Here $[O/H] = 12 + \log(O \times 0.00049)$ and $[Fe/H] = 12 + \log(\text{Fe} \times 0.0000269)$, using the solar Wilms values for O/H and Fe/H. As seen in the plots, the errors in oxygen abundance are much smaller for a given number of counts compared to the errors in iron abundance. Further, the upper limits on the oxygen abundance continue to be meaningful through 2000 counts. This is not true for the iron abundances, where the error bars extend through the entire range of allowed values ($\text{Fe}/\text{H} = 0.0\text{--}5.0$, or $[Fe/H]$ up to 8.13). Thus, our simulations show us that the iron abundance (from measurements of the Fe L-shell edge at 851 eV with the tbvarabs model) requires at least 5000 counts to be detected. At 5000 counts the model-derived value ($\text{Fe}/\text{H} = 1.36$) is meaningful; however, the errors extend throughout the entire allowable range ($\text{Fe}/\text{H} = 0.0\text{--}5.0$). The oxygen abundance (from measurements of the O K-shell edge at 542 eV with the tbvarabs model) is detected down to 2000 counts, but with large errors below 10,000 counts.

From Table 8, we find that the same trends described in § 4.1 are present in our simulations, namely, there is little variation between the model-derived abundances and column densities. A comparison of the mean n_{H} and oxygen abundance values shows $\approx 2\%$ difference between the `grad` and `diskbb` model. The `bbody` n_{H} values are roughly 26% higher, while the oxygen abundances are $\approx 11\%$ higher. Comparing the 40,000 and 200,000 count spectra for the iron abundance, we find that the `grad` and `diskbb` model values differ by $\approx 12\%$ while the `bbody` model results are larger by a factor of 50%. While the `bbody` model yields lower column densities and higher abundances, the `diskbb` and `grad` models are in agreement. The differences in the `bbody` results are low for the column density and oxygen abundance but appeared significant for the iron abundance.

APPENDIX B

COMPARISON WITH SAS 6.5 DATA PROCESSING

We reprocessed the pn data in this study with the new version of SAS (6.5), in order to observe the effects different SAS versions would have on our results. After processing the data (with `epchain`), we extracted spectra as described in § 2. The spectra were then fitted with the $\text{tbabs}^*\text{tbvarabs}^*(\text{grad}+\text{pow})$ model. Note that the edge model was not needed to correct for differences in calibration between the MOS and pn since we only fitted pn spectra. Since the MOS data were not added, the counts for the pn-only spectra are lower than the MOS+pn spectra. Thus, we excluded spectra for sources with less than 5000 counts in the pn. The results are shown in Table 9, ordered by number of counts.

In Figure 13 we plot a comparison of the X-ray hydrogen column densities and oxygen abundances (both from the tbvarabs model) from SAS version 6.0 and 6.5. From these plots, we find that the SAS 6.0 n_{H} values are slightly lower but consistent with the

TABLE 9
SPECTRAL FITS FOR EPIC SPECTRA WITH THE `tbabs*tbvarabs*(grad+pow)` MODEL

Source	n_{H}^{a} (10^{22} cm^{-2})	O Abundance ^b	Fe Abundance ^b	Mass (M_{\odot})	$\dot{M}/\dot{M}_{\text{Edd}}^{\text{c}}$	Γ	χ^2/dof	Counts ^d
Holm IX XMM1.....	$0.18^{+0.02}_{-0.02}$	$1.67^{+0.12}_{-0.14}$	$1.61^{+0.76}_{-0.88}$	442^{+110}_{-91}	$0.08^{+0.02}_{-0.02}$	$1.47^{+0.02}_{-0.02}$	1637.1/1532	171210
	$0.18^{+0.05}_{-0.04}$	$1.46^{+0.41}_{-0.49}$	$1.84^{+2.23}_{-1.84}$	258^{+327}_{-164}	$0.10^{+0.12}_{-0.06}$	$1.68^{+0.08}_{-0.09}$	477.8/486	14996
Holm II XMM1	$0.12^{+0.01}_{-0.01}$	$1.13^{+0.14}_{-0.14}$	$0.0^{+0.24}_{-0.0}$	100^{+26}_{-23}	$0.11^{+0.03}_{-0.03}$	$2.45^{+0.06}_{-0.05}$	939.3/932	150290
	$0.12^{+0.03}_{-0.02}$	$1.19^{+0.51}_{-0.68}$	$3.08^{+1.92}_{-3.08}$	272^{+232}_{-163}	$0.07^{+0.06}_{-0.03}$	$2.31^{+0.12}_{-0.13}$	362.4/368	13983
M33 X-8	$0.08^{+0.03}_{-0.03}$	$1.21^{+0.37}_{-0.48}$	$0.0^{+1.15}_{-0.0}$	$7.23^{+0.68}_{-0.63}$	$0.96^{+0.06}_{-0.06}$	$2.12^{+0.25}_{-0.26}$	714.9/749	46579
M81 XMM1	$0.48^{+0.13}_{-0.16}$	$1.22^{+0.11}_{-0.15}$	$1.61^{+0.58}_{-1.09}$	$9.13^{+0.73}_{-0.83}$	$3.29^{+0.31}_{-0.31}$	$3.31^{+0.68}_{-0.95}$	865/811	42188
N4559 X-7	$0.16^{+0.04}_{-0.03}$	$0.52^{+0.42}_{-0.52}$	$0.0^{+1.08}_{-0.0}$	1000^{+1057}_{-604}	$0.04^{+0.05}_{-0.03}$	$2.16^{+0.07}_{-0.08}$	407.1/359	12492
NGC 5204 XMM1	$0.04^{+0.03}_{-0.01}$	$1.28^{+1.41}_{-1.28}$	$0.0^{+5.0}_{-0.0}$	120^{+146}_{-80}	$0.04^{+0.05}_{-0.02}$	$1.94^{+0.10}_{-0.13}$	305.7/323	9991
	$0.09^{+0.03}_{-0.03}$	$1.60^{+0.79}_{-0.99}$	$0.0^{+2.43}_{-0.0}$	254^{+194}_{-104}	$0.10^{+0.04}_{-0.04}$	$1.90^{+0.22}_{-0.25}$	244.8/278	7503
NGC 4559 X-10	$0.11^{+0.03}_{-0.03}$	$1.47^{+0.63}_{-0.53}$	$0.0^{+2.0}_{-0.0}$	$7.06^{+3.45}_{-3.0}$	$4.76^{+2.65}_{-2.83}$	$2.22^{+0.58}_{-0.29}$	266.4/328	8834
NGC 300 XMM1	$0.09^{+0.03}_{-0.03}$	$2.58^{+0.81}_{-0.77}$	$0.0^{+1.67}_{-0.0}$	160^{+153}_{-81}	$0.01^{+0.01}_{-0.01}$	$2.46^{+0.15}_{-0.16}$	278.9/237	6771
NGC 1313 XMM3	$0.40^{+0.16}_{-0.12}$	$1.70^{+0.27}_{-0.34}$	$3.0^{+1.46}_{-1.77}$	907^{+1477}_{-604}	$0.06^{+0.14}_{-0.11}$	$2.25^{+0.09}_{-0.17}$	246.2/232	6237
NGC 5408 XMM1	$0.05^{+0.03}_{-0.03}$	$2.43^{+1.42}_{-1.32}$	$5.0^{+0.0}_{-5.0}$	840^{+361}_{-245}	$0.11^{+0.04}_{-0.03}$	$2.24^{+0.31}_{-0.30}$	174/187	5928
NGC 4631 XMM1	$0.28^{+0.12}_{-0.07}$	$0.41^{+0.52}_{-0.41}$	$0.0^{+2.5}_{-0.0}$	$6.73^{+2290}_{-6.4}$	$0.72^{+1.15}_{-0.72}$	$1.95^{+0.24}_{-0.40}$	215.4/189	4830

^a Hydrogen column density determined from `tbvarabs`. The Galactic value of n_{H} was fixed to the Dickey & Lockman (1990) value with the `tbabs` model.

^b Element abundance relative to the Wilms solar abundance from the `tbvarabs` model.

^c Ratio of mass accretion rate from the `grad` model to Eddington accretion rate (see § 4).

^d Total number of photon counts from the pn detector.

SAS 6.5 observations. The [O/H] values are slightly higher for SAS 6.0 but are also consistent. Since the hydrogen column density and oxygen abundance values are consistent between both versions, we did not find it necessary to recalculate EPIC spectral parameters for the sources. Thus, the values quoted in the paper are from the data processed with SAS version 6.0. While the error bars for the SAS 6.5 Fe abundances are larger, due to the lower number of counts in the pn alone, within the errors the values are consistent with the SAS 6.0 values. For the highest number of count sources (Holmberg IX XMM1 and Holmberg II XMM1), the fits for the longest observations yielded the same Fe abundance for Holmberg II XMM1 ($\text{Fe}/\text{H} = 0.0$ ranging to ≈ 0.20) and consistent values for Holmberg IX XMM1 (the SAS 6.0 values $[\text{Fe}/\text{H}]$ from 2.19 to 1.94) were well within the SAS 6.5 values $[\text{Fe}/\text{H}]$ from 2.37 to 0.75).

We also note that the release notes for SAS version 6.0 (Carlos Gabriel & Eduardo Ojero; available online) indicate no substantial differences in the EPIC responses. Therefore, the edge model correction quoted in Baumgartner & Mushotzky (2006) is adequate and did not need to be recalculated from SAS 5.4 (as in Baumgartner & Mushotzky 2006) to SAS 6.0.

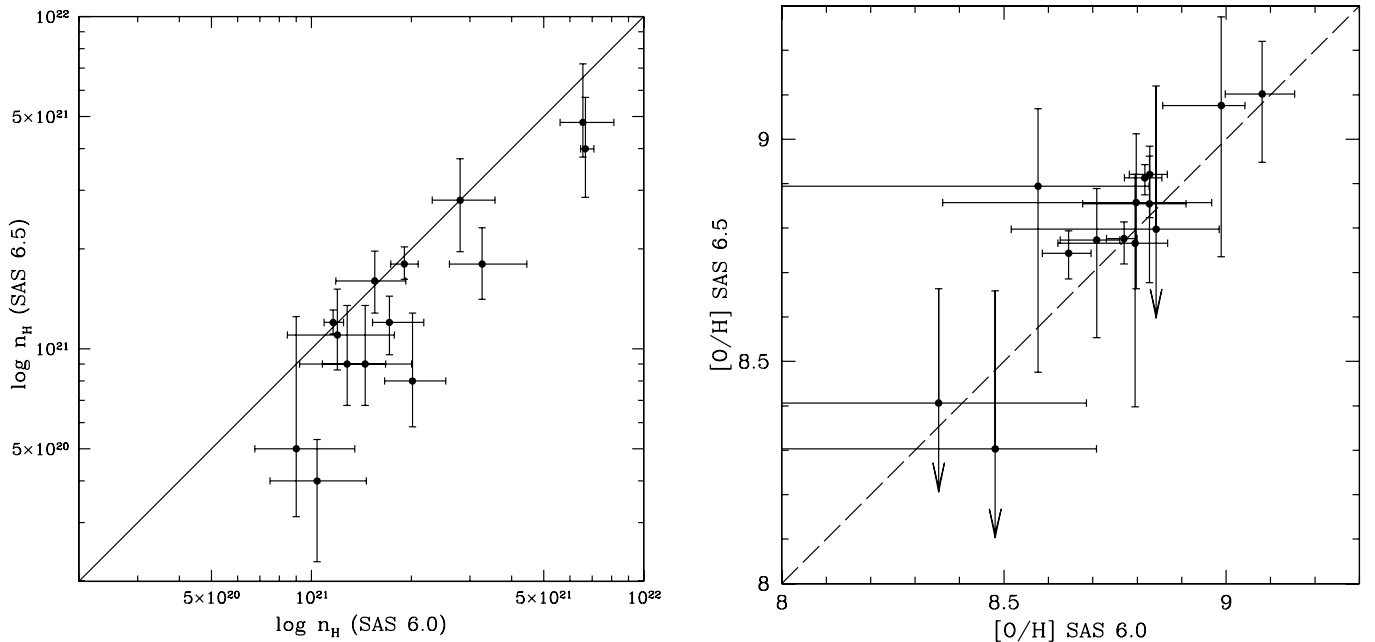


FIG. 13.—Comparison of the galactic/ULX hydrogen column density obtained from the `tbvarabs` model for SAS 6.0 processed data (from Table 2) vs. SAS 6.5 processed data (from Table 9) (*left*) and comparison of the similarly obtained [O/H] values (*right*). From these plots, we find that the SAS 6.0 n_{H} and [O/H] values are consistent with the SAS 6.5 values. The SAS 6.0 column densities are slightly lower than the SAS 6.5 values, and the SAS 6.0 oxygen abundances are slightly higher, on average. The lines in the plot represent agreement between the SAS 6.0 and 6.5 values. Arrows are used to indicate fits where the lower limit for the oxygen abundance extends below the plotted range.

REFERENCES

- Anders, E., & Ebihara, M. 1982, *Geochim. Cosmochim. Acta*, 46, 2363
- Baumgartner, W. H., & Mushotzky, R. F. 2006, *ApJ*, 639, 929
- Braun, R. 1995, *A&AS*, 114, 409
- Calzetti, D., & Kinney, A. L. 1994, *ApJ*, 429, 582
- Cropper, M., Soria, R., Mushotzky, R. F., Wu, K., Markwardt, C. B., & Pakull, M. 2004, *MNRAS*, 349, 39
- Dickey, J. M., & Lockman, F. J. 1990, *ARA&A*, 28, 215
- Ebisawa, K., Mitsuda, K., & Hanawa, T. 1991, *ApJ*, 367, 213
- Garcia, J., Mendoza, C., Bautista, M. A., Gorczyca, T. W., Kallman, T. R., & Palmeri, P. 2005, *ApJS*, 158, 68
- Garnett, D. R. 2002, *ApJ*, 581, 1019
- Gierliński, M., & Done, C. 2004, *MNRAS*, 349, L7
- Goad, M. R., Roberts, T. P., Reeves, J. N., & Uttley, P. 2006, *MNRAS*, 365, 191
- Goncalves, A. C., & Soria, R. 2006, *MNRAS*, 371, 673
- Hanawa, T. 1989, *ApJ*, 341, 948
- Ho, L. C., Filippenko, A. V., & Sargent, W. L. M. 1997, *ApJS*, 112, 315
- Juett, A. M., Schulz, N. S., & Chakrabarty, D. 2004, *ApJ*, 612, 308
- Kaaret, P., Corbel, S., Prestwich, A. H., & Zezas, A. 2003, *Science*, 299, 365
- Kong, X., et al. 2000, *AJ*, 119, 2745
- Long, K. S., Charles, P. A., & Dubus, G. 2002, *ApJ*, 569, 204
- McClintock, J. E., Narayan, R., & Rybicki, G. B. 2004, *ApJ*, 615, 402
- Miller, B. W. 1995, *ApJ*, 446, L75
- Miller, J. M., Fabbiano, G., Miller, M. C., & Fabian, A. C. 2003, *ApJ*, 585, L37
- Miller, J. M., Fabian, A. C., & Miller, M. C. 2004, *ApJ*, 607, 931
- Mitsuda, K., et al. 1984, *PASJ*, 36, 741
- Morrison, R., & McCammon, D. 1983, *ApJ*, 270, 119
- Paturel, G., Fouque, P., Bottinelli, L., & Gouguenheim, L. 1989, *A&AS*, 80, 299
- Pilyugin, L. S., Vílchez, J. M., & Contini, T. 2004, *A&A*, 425, 849
- Predehl, P., & Schmitt, J. H. M. M. 1995, *A&A*, 293, 889
- Reilman, R. F., & Manson, S. T. 1979, *ApJS*, 40, 815
- Roberts, T. P., Warwick, R. S., Ward, M. J., Goad, M. R., & Jenkins, L. P. 2005, *MNRAS*, 357, 1363
- Ross, R. R., & Fabian, A. C. 2005, *MNRAS*, 358, 211
- Searle, L. 1971, *ApJ*, 168, 327
- Stobart, A.-M., Roberts, T. P., & Wilms, J. 2006, *MNRAS*, 368, 397
- Swartz, D. A., Ghosh, K. K., Tennant, A. F., & Wu, K. 2004, *ApJS*, 154, 519
- Swaters, R. A., van Albada, T. S., van der Hulst, J. M., & Sancisi, R. 2002, *A&A*, 390, 829
- Takano, M., Mitsuda, K., Fukazawa, Y., & Nagase, F. 1994, *ApJ*, 436, L47
- Tremonti, C. A., et al. 2004, *ApJ*, 613, 898
- Vogler, A., Pietsch, W., & Bertoldi, F. 1997, *A&A*, 318, 768
- Walsh, J. R., & Roy, J.-R. 1997, *MNRAS*, 288, 726
- Wilms, J., Allen, A., & McCray, R. 2000, *ApJ*, 542, 914
- Winter, L. M., Mushotzky, R., & Reynolds, C. S. 2006, *ApJ*, 649, 730 (Paper I)